FABRICATION AND CHARACTERIZATION OF OPTICALLY EMISSIVE MICRORESONATORS

A Thesis
Presented to
The Academic Faculty

by

Eric Steven Mansfield

In Partial Fulfillment
of the Requirements for the Degree
Masters of Science in the
School of Materials Science and Engineering

Georgia Institute of Technology
August, 2011

COPYRIGHT 2011 ERIC MANSFIELD

FABRICATION AND CHARACTERIZATION OF OPTICALLY EMISSIVE MICRORESONATORS

Approved by:

Dr. Joseph W. Perry, Advisor
School of Chemistry and Biochemistry
Georgia Institute of Technology

Dr. Kenneth H. Sandhage
School of Materials Science and Engineering
Georgia Institute of Technology

Dr. Christopher J. Summers
School of Materials Science and Engineering
Georgia Institute of Technology

Date Approved: April 29, 2011

To my teachers, who made everything possible.

ACKNOWLEDGEMENTS

I wish to thank Professor Joe Perry for his guidance, insightful questions and support through conducting my thesis research.

I wish to thank every member of the Perry Research Group for their encouragement, good humor and technical input. In particular, I would like to thank Vincent Chen, Dr. Joel Hales, Dr. Mohan Kathaperumal, Nikolay Makarov, and Nathan Jarnagin for many fruitful discussions.

I am grateful for the spectroscopic characterization assistance provided by the Josef Zyss group at ENS Cachan.

This work was generously funded through the Air Force Office of Sponsored Research.

TABLE OF CONTENTS

LIST OF TABLES

LIST OF FIGURES

LIST OF SYMBOLS AND ABBREVIATIONS

λ	wavelength (nm)
n	index of refraction
m	an integer greater than 0
p	the integer number of sides on a polygon
MPL	Multi-photon Lithography

SUMMARY

Microresonators are an area of current and growing interest with applications as light sources, lasers, sensors and taggarts. Microresonators are devices that confine light in small volumes through total internal reflection. Introducing an emissive species into a microresonator allows for resonance enhanced emission at frequencies where the spectrum of the emissive species overlaps with the resonant frequencies of the microresonator. Previous research has led to a good understanding of these phenomena in 1D and 2D microresonators, but many 3D microresonator geometries have not yet been investigated.

One hitherto unpublished microresonator geometry is the cube. The cube offers a predicted limited set of resonant frequencies and is facile to fabricate. Fabrication was accomplished via 3D multi-photon lithography, a method for 3-D creating free-form, true 3D polymeric microstructures. There were four fundamental challenges in creating a cubic microresonator. The first was developing the tools to reproducibly and precisely fabricate cubic microresonators. Second, it was necessary to refine the device fabrication process to minimize losses in the device. Third, an emissive species had to be integrated into the device to transform it into an active microresonator. The selected emissive species had to be optically active following the device fabrication process. Lastly, the devices had to be spectroscopically characterized to demonstrate the existence of resonant cavity modes in the device.

CHAPTER 1: INTRODUCTION

Microresonators are an area of current and growing interest with applications as light sources, lasers, sensors and taggarts [1, 2]. Microresonators are devices that confine and circulate resonant light in a small volume. The resonant frequencies in a given microresonator are tunable via device geometry. The most fundamental microresonator confines light along a single axis and is an integral part of a every laser [3]. It is possible to create microresonators, which confine light in two dimensions (2-D). 2-D microresonators may be created in any arbitrary shape or regular polygon [4]. 2-D microresonators make use of the total internal reflection of light to confine resonant modes of light. As a result, the material index of refraction serves to limit the possible modes supported by a given geometry. The square microresonator is a particularly interesting example of this ; when created of a material of an index less than 2.0, the only family of resonant modes resembles a square path inscribed in the device. Other notable 2-D microresonators include ring and toroidal resonantors, which are both being investigated for applications in optical switching [2, 5].

Work has been done to extended microresonators from 2D to 3D. The most well-characterized 3D microresonator is the microsphere. Microspheres are fabricated by heating silica fibers until spheres of molten glass form on their ends [5, 6]. It is possible to create microresonators with extremely high sensitivity to detect the presence of particles as small as a single virus [7]. The microsphere is one of the few microresonators capable of supporting complex 3D mode paths.

An interesting next step in the development of 3D microresonators would be the creation of polyhedral microresonators. The creation and successful demonstration of emission in polyhedral microresonators has not been previously reported in the literature.

As mentioned above in the discussion of the number of modal families in a 2D microresonator, there was only a single geometry that limited the number of mode families to a single option; this geometry was a square. Making similar considerations for regular polyhedral microresonators, it is conceivable that a cubic microresonator would only support a single family of resonant modes confined on separate orthogonal planes inside the device.

Optical microresonators are typically fabricated utilizing photolithography of doped semiconductor materials [8]. However, it is also possible to create microresonators through photolithography of polymers, or by shaping silica fibers with heat [6]. A novel alternative to traditional fabrication methods is to use Multi-Photon Lithography (MPL). MPL is a method for rapidly creating free-form, true 3D structures with features as small as 100 nm using a highly spatially-confined polymerization initiated by resonant photons [9]. The polymerization system consists of free acrylate and diacrylate monomers along with an initiator dye capable of causing multi-photon polymerization. MPL polymerization occurs when a sufficient number of resonant photons are incident on the initiator molecule simultaneously. The probability of two photons causing a resonant energy transition is extremely low under unfocused light; however, the probability is significantly higher in the focal volume of the laser. As a result, it is possible to utilize the focal volume of the laser as a fine writing implement to cause selective polymerization [10].

MPL offers several advantages relative to conventional photolithography techniques. First, MPL can create complex free-form true 3D structures of arbitrary design without masks. These structures can be on the order of tens to hundreds of

micrometers with features down to 100 nm [9]. Lastly, a large range of emissive species may be integrated into MPL fabricated structures ranging from organic dyes to rare earth metal complexes. The integrated species can be excited via an external light source to cause emission at another frequency. This ability allows MPL to create optically active devices.

There will be several key objectives that must be met for successful device demonstration:

1) **Fabricate a three-dimensional cubic optical microresonator:** Using MPL, cubic microresonators must be reproducibly fabricated to desired dimensions.
2) **Increase the quality factor**, Q, of the microresonator. The quality factor is the ratio of the energy stored in a microresonator to the energy lost by the device per unit time. A large quality factor is desirable because it will result in strong, narrow band emission from the device. The roughness of the device surfaces plays a crucial role in the overall microresonator Q. Rough surfaces lead to excessive scattering and a low Q; while, smooth surfaces minimize loss and increase device Q. Consequently, one of the main foci of this work will be to minimize device roughness arising from the fabrication process.
3) **Integrate an emissive species** into the microresonator. In order to observe the supported cavity modes in the device, it is necessary to integrate a strongly emissive species in the device that is capable of being excited from an external light source. In addition, the species must be soluble in the MPL starting solution and remain optically active following all steps of the MPL process.

4) **Demonstrate the existence of cavity modes.** Spectroscopic characterization involves device excitation with an intense light (i.e. a laser) and observation of the emitted light from the device. The desired emission is a series of sharp emission peaks, which is indicative of stimulated emission and lasing.

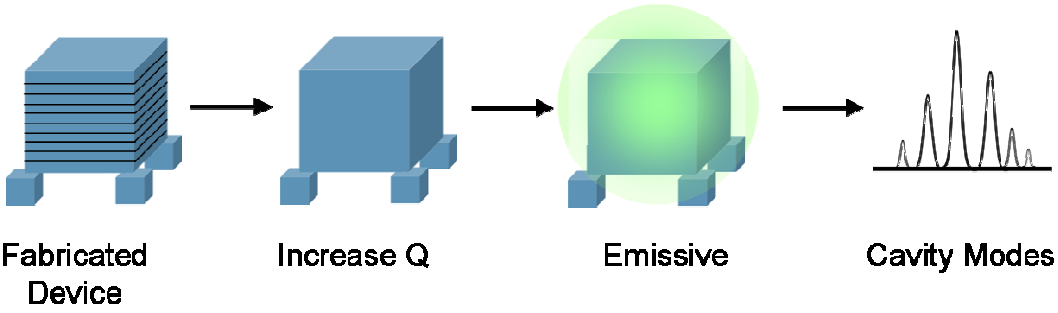

Figure 1.1: The four goals of the research illustrated: 1) fabricating a device to desired dimmensions 2) increasing the quality factor, Q, via surface roughness reduction, 3) integration of an emissive species in the device and finally 4) observation of cavity modes in the far field.

CHAPTER 2: BACKGROUND

Microresonator Theory

Optical microresonators are devices that confine, intensify and store light [2]. Optical resonators may be classified in terms of the number of dimensions along which light is confined, e.g. 1-D, 2-D and 3-D. The simplest 1-D optical microresonator, illustrated in figure 2.1a, consists of two plane parallel mirrors separated by a distance L, referred to as a Fabry-Perot resonator. Light waves travel along the longitudinal axis of the cavity and are reflected between two plane parallel mirrors. Standing waves develop within the cavity as a result of constructive and destructive interference effects. The standing waves are half wavelength multiples of the cavity length, L. This relationship is described in 1-D standing wave equation, where m is an integer great than 0. Thus the first resonant mode in a 1-D cavity, as illustrated in 2.1b, is half a wave, $\lambda=2L$. The second resonant mode is a complete wave, depicted in 2.1c, $\lambda=L$ [1, 3].

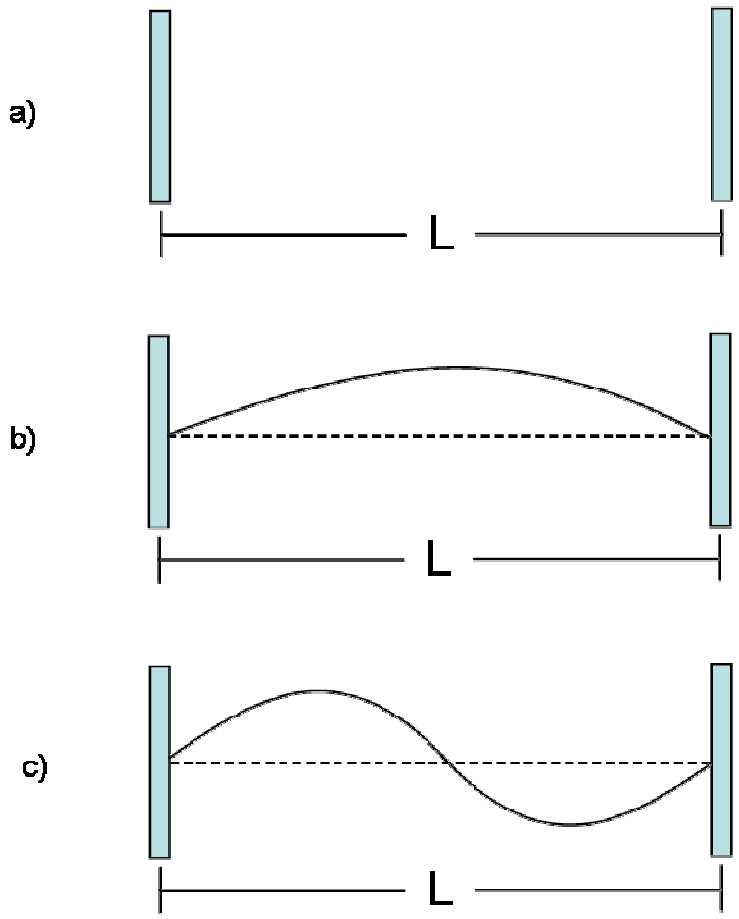

Figure 2.1: a) a 1-D microcavity consisting of two plane parallel mirrors, b) the first resonant mode of the microresonator (m=1) λ=2L, c) the second resonant mode of the microresonator (m=2) λ=L

$$m\frac{\lambda}{2} = L$$

where, m=an integer greater than 0.

The equation above describes the set of all possible wavelengths that can resonantly circulate in a 1-D cavity. Figure 2.2 depicts a distribution of modes plotted as a function of wavelength, λ. The idealized modes appear as a series of infinitely thin peaks with a height of infinity. The peak to peak distance between the modes is referred to either as the Free Spectral Range (FSR) or the modal spacing.

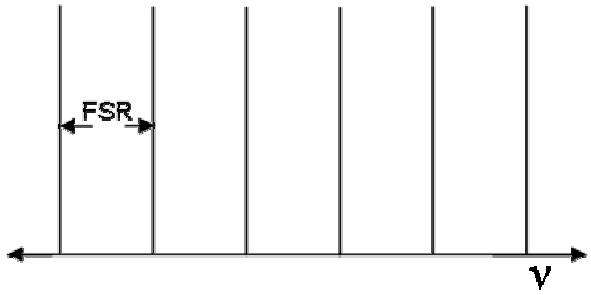

Figure 2.2: Ideal mode structure inside a microcavity. The sharp lines represent the resonant wavelengths of the cavity. The distance between the lines is known as the Free Spectral Range (FSR) or modal spacing.

The FSR for a given microresonator is constant across the entire frequency domain; however, it is important to note that the modal spacing is not constant when discussing the wavelengths of the resonant. Due to this property, long wavelength emissions from a microresonator are further spaced apart than shorter wavelengths. Figure 2.3 illustrates the modal spacing in a 5 μm 1-D microresonator between λ=200 to λ=1000 nm. At λ=200 nm, the modal spacing is 3 nm. At the end of the wavelength range, at λ=966 nm, the modal spacing is 69 nm. As a result of the increase in modal spacing, if the goal of device fabrication is to build a single-mode cavity, then a longer wavelength emitter is preferred.

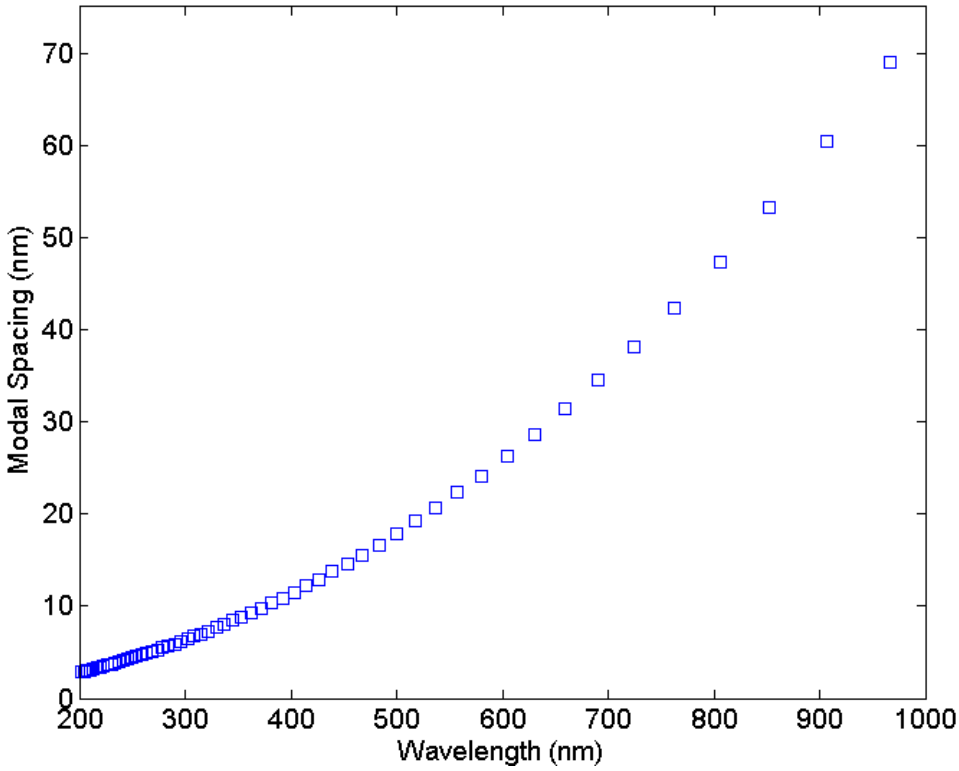

Figure 2.3: The modal spacing of a (L=5 μm) 1-D microresonator plotted as a function of wavelength. Notice how the modal spacing dramatically increases from 3 nm at λ=200 nm to 69 nm at λ=966 nm. This plot can be reproduced by modifying ModalSpacing.m in Appendix A.

The modal spacing is also a function of the physical dimensions of the microresonator. Figure 2.4 shows the modal spacing for various 1-D microresonator edge lengths plotted at λ=500 nm. Considering a fixed wavelength, it can be seen that as the length of the 1-D cavity decreases, the spacing between the modes increases. Thus if the goal of device fabrication is to build a single mode cavity, then a smaller cavity is preferred.

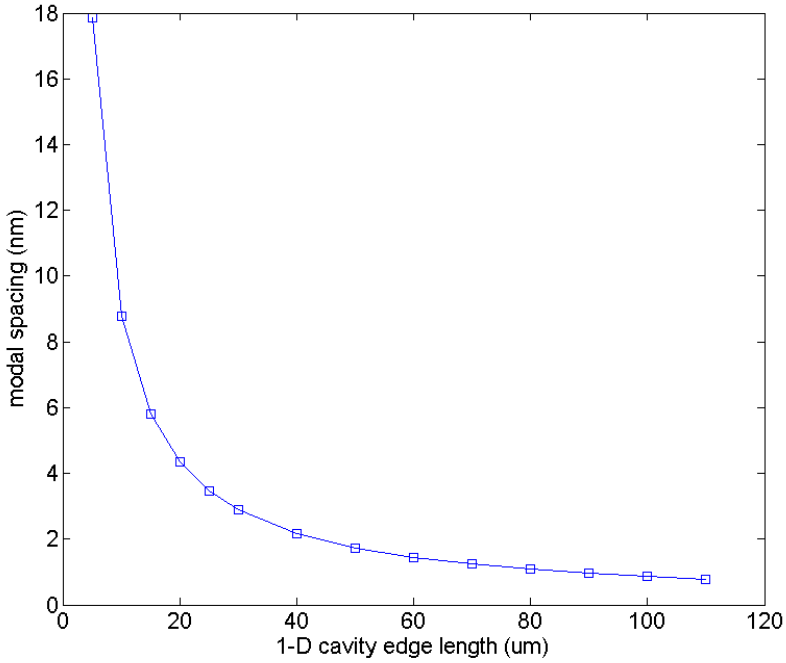

Figure 2.4: Modal spacing at λ=500 nm for 1-D microresonators with lengths of 5, 10, 20,40, 60, 80 and 100 μm. By considering a single wavelength, it can be clearly seen that as cavity length decreases, the modal spacing increases. This plot can be reproduced with ModalSpacing.m in Appendix A.

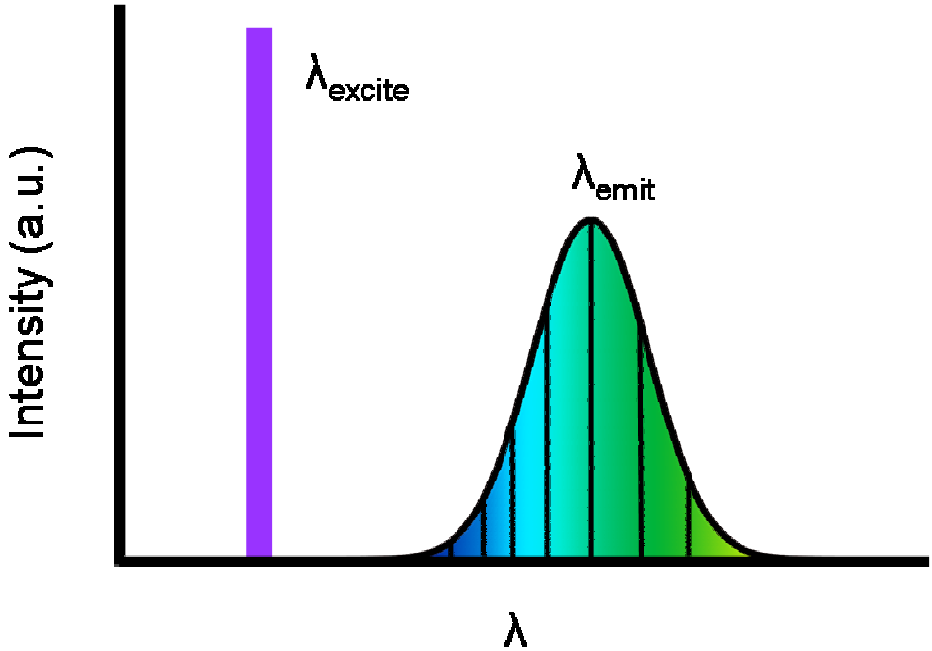

Figure 2.5: Optical gain medium in a microresonator excited at λexcite resulting in broadband emission peaking at λemit. The vertical lines inside the emission spectrum represent the resonant modes of the microresonator.

A microcavity is a passive device; however adding a chromophore to its interior results in the creation of an active device, a microresonator. As illustrated in Figure 2.5, exciting this device with a laser of λ=λexcite results in emitted light over a range of wavelengths. The emission curve of the laser dye overlaps the sharp resonant modes of the cavity, described above in the 1-D cavity standing wave equation. The resulting emission spectrum from the microresonator is the product of the resonant modes and the emission curve of the dye; hence it resembles a rounded Gaussian distribution (illustrated in figure 2.6).

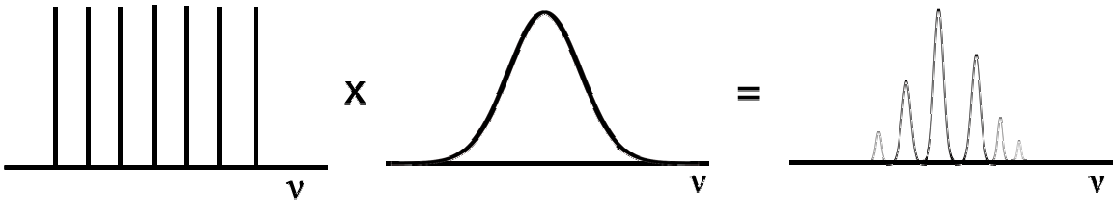

Figure 2.6: The emission spectrum of a microresonator is a product of the cavity modes and the emission curve of the emissive species in the microresonator. The resultant emission spectrum therefore is a modulated version of the emission curve.

An important figure of merit for a microresonator is the quality factor, Q. It is a measure of the ratio of the energy stored in a microresonator to the dissipated energy. Pragmatically, Q provides a measure of the relative energetic threshold for lasing and the brightness of resulting emission. A high Q device has a low threshold and a narrow, bright emission spectrum. A low Q device demonstrates the opposite. Q is most readily computed as the wavelength or frequency of a resonant peak divided by its width at half maximum:

$$Q = \frac{EnergyStored}{EnergyDissipated} = \frac{\nu_{resonant}}{\Delta\nu_{1/2}} = \frac{\lambda_{resonant}}{\Delta\lambda_{1/2}}$$

Where, $\Delta\nu_{1/2}$ and $\Delta\lambda_{1/2}$ are the peak width at half maximum. It is desirable to increase Q . Figure 2.7 shows three emission peaks from a hypothetical microresonator. The area under the peaks, the excitation energy, is the same for all three peaks. Note how the left peak has a large width and low maximum value. Increasing Q results in a narrower peak with a great maximum intensity. Further increasing Q creates an even stronger, narrow peak. Increasing the microresonator Q increases the intensity (brightness) of the emitted light, lowers the lasing threshold allowing the device to be excited at lower powers and causes narrowing of the spectral emission peaks.

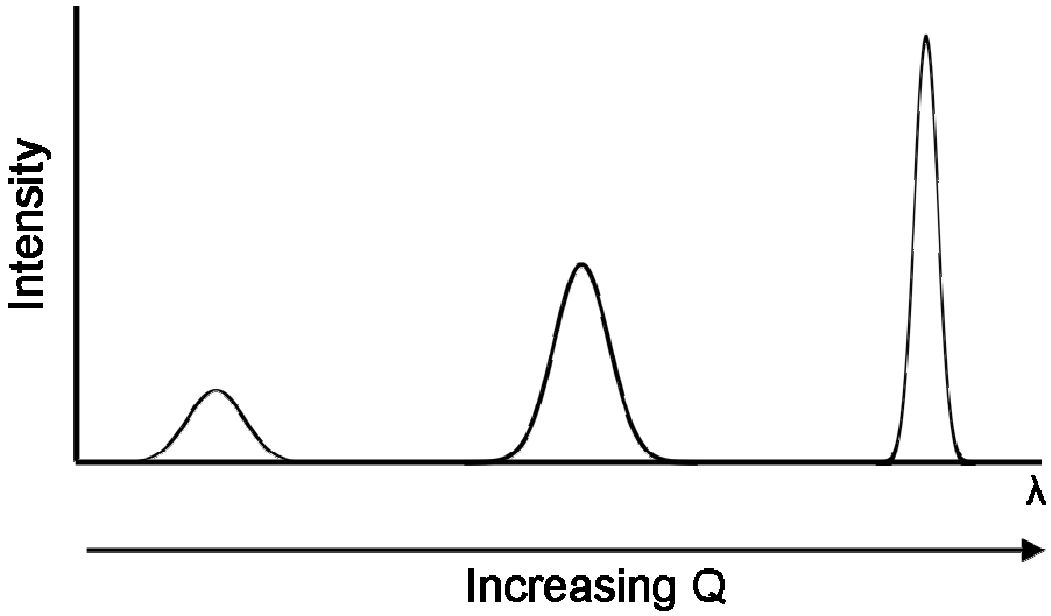

Figure 2.7: Three emission peaks from a hypothetical microresonator. The area under the peaks, the excitation energy, is the same for all three peaks. Note how the left peak has a large width and low maximum value. Increasing Q results in a narrower peak with a great maximum intensity. Further increasing Q creates an even taller, narrow peak. The taller sharp peak has greater brightness and a lower lasing threshold.

In the 1-D cavity, resonant light only travels along a single axis between highly reflective mirrors; however, highly reflective mirrors are not the only means for confining light. Light can also be confined in a volume through use of total internal

reflection, whereby light rays incident on the boundaries of the cavity at angles greater than the critical angle are fully internally reflected. The critical angle is expressed as:

$$\Theta_{crit} = \arcsin \frac{n_{surr}}{n_{mat}}$$

Where n_{mat} and n_{surr} denote the refractive indices of the material and the surrounding, respectively. Figure 2.8 iterates the angle of incidence of a light ray inside a higher index material (n=1.5) traveling to a lower index (n=1). From left to right, the ray approaches first normal to the boundary with complete transmission. As the angle grows, the majority of the ray passes through the boundary and is refracted. In addition, a smaller portion of the light is internally reflected. When the incidence angle equals the critical angle, the light ray is totally internally reflected. All subsequent angles greater than the critical angle are also totally internally reflected.

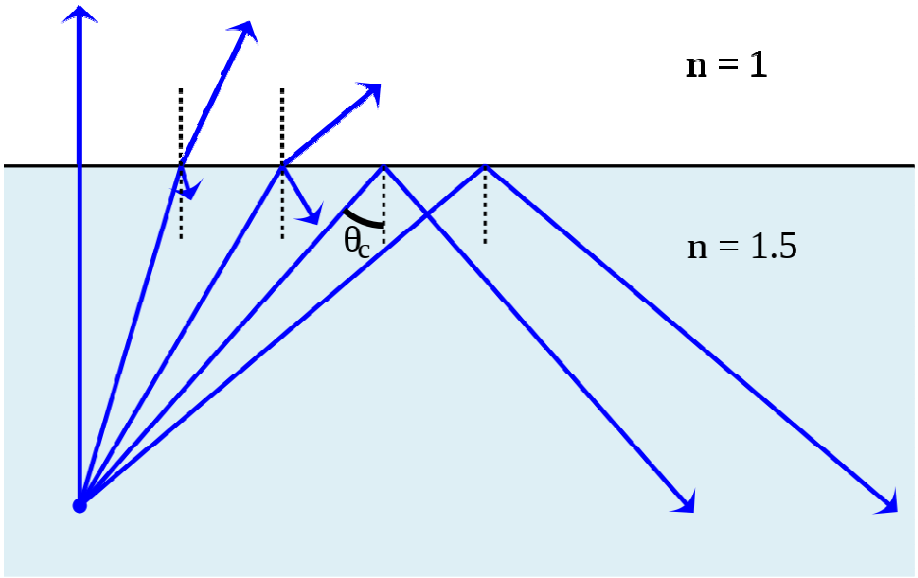

Figure 2.8: Iterative changes to the angle of incident of a light ray on a high to low index boundary. As the angle of incidence equals and exceeds the critical angle, the ray of light is internally reflected. Figure courtesy of Wikipedia

One notable device that makes use of TIR to confine and guide light is the fiber optic waveguide. In a fiber optic waveguide, light is reflected internally at angles greater than the critical angle off parallel longitudinal boundaries, causing light to propagate along the longitudinal axis of the fiber optic. Fiber optic waveguides are not microresonators, but 2-D microresonators make use of the same TIR phenomena to confine light.

Using TIR to confine light in microresonator allows for facile creation of complex 2D geometries. Two-dimensional microresonators share many common properties with 1-D microresonator except as their name suggests, they support light propagation in two dimensions rather than just one. An interesting property that arises from stable 2D light confinement is a class of modes known as whispering gallery modes (WGM) that trace the perimeter of the microresonator at glancing angles.

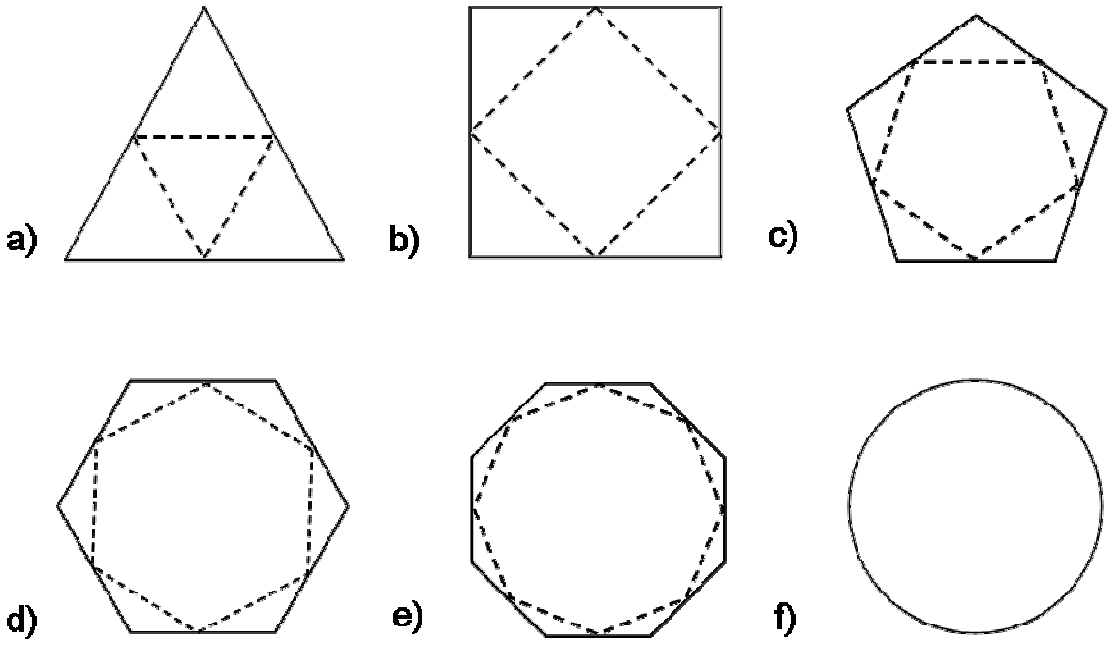

Figure 2.9: Evolution of whispering gallery modes in regular polygonal microresonators. As the number of sides, p, approaches infinity, whispering gallery modes are exclusively confined to the outer boundaries of the microresonator. The resonant path is depicted as a dashed line inside solid boundaries. At the extreme of the circle, the ray trace diagram fails to describe the complexity of the WGM, and is not a circle inscribed on another circle.

The evolution of whispering gallery modes, depicted in 2.9, can be considered in terms of increasing the number of sides, *p*, of a regular polygon. As *p* increases, the WGM path evolves to be closer to the boundary of the microresonator. At the same time as *p* increases, the number of vertices of the polygon increase making it easier for totally internally reflected light to propagate. Eventually, the number of sides becomes infinite and the polygon is a circle. As *p* increases, the number of possible stable modal paths inscribed in a *p*-sided polygon increase. This means that for polygons with a large *p*, multiple families of modes can exist simultaneously. The emission spectra of such polygons would be the product of multiple families.

For example, given a series of *p*-sided 2D regular polygonal microresonators fabricated of PMMA with an index of 1.49; the critical angle is 42°. In this series, plotted in figure 2.10, microresonators with $p \geq 5$, multiple modal families could exist simultaneously. For instance, it is possible to inscribe a rectangular family as well as a pentagonal family in a pentagonal microresonator. To build a single family device, the only possible regular polygon would be a square ($p=4$). The smallest possible polygon, the triangle ($p=3$), would be incapable of TIR, and hence could not form a functional microresonator.

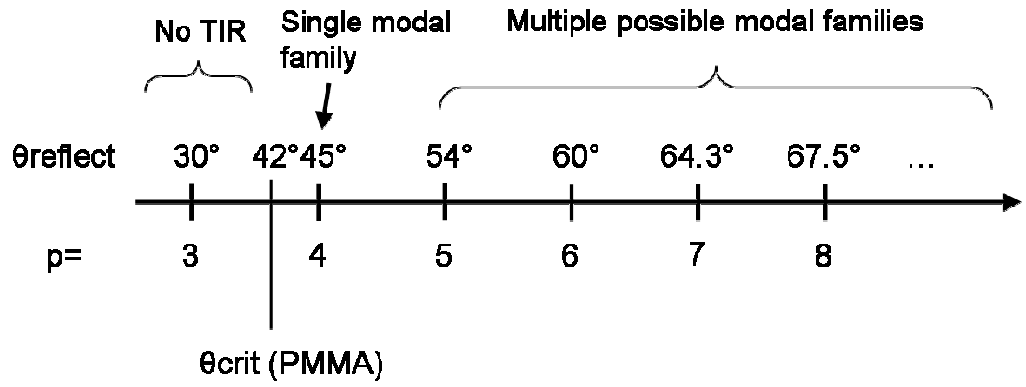

Figure 2.10: The number line above shows the angle relative to the normal of an edge for reflected light confined in a polygon of *p*-sides. At θreflect<42° (the critical angle for PMMA), there are no totally internally confined modes of light. At θreflect>42°, light can be confined via TIR. Note that the square (*p*=4) is unique in its ability to sustain only one modal family, the inscribed square.

The square is only able to support a single family of resonator modes due to its geometry and the critical angle. In the square, the properties of alternate interior angles are critical in limiting the allowed angles for TIR. A ray of light in a square will always be reflected at an angle of θ or its complimentary angle (90 degrees –θ) [11]. Figure 2.11 shows the critical angle and its compliment ($90-\theta_{crit}$). The two curves intersect at a refractive index contrast of 1.41. For all index contrast values less than 1.41, no rays of light can be confined in the square via total internal reflection. At a refractive index contrast of 1.41 and above, TIR modes exist within the square. As the index contrast ratio increases, a larger range of angles allows light confinement TIR. For an index ratio of 2.0, angles between 30 and 60 degrees are possible. For MPL fabricated structures with a predicted index ratio of 1.49 (based on PMMA v. air), angles between 42.2 and 47.8 are possible. The actual index of the fabricated devices as measured from a 100 mM Coumarin 481 doped film is 1.53, so the index of PMMA is a good approximation.

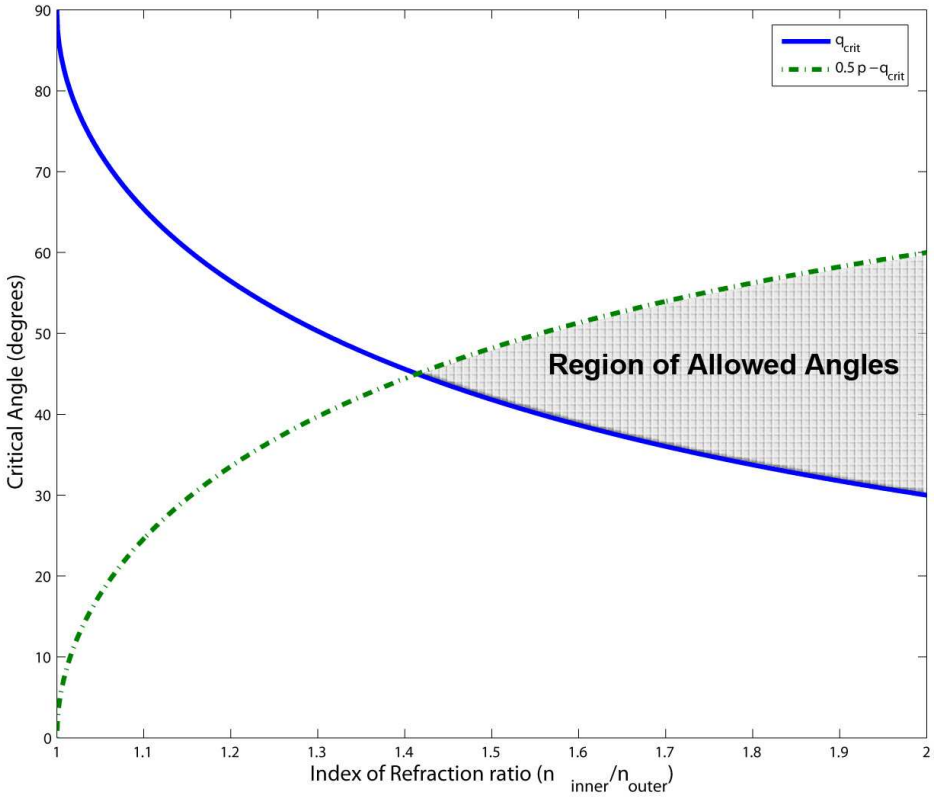

Figure 2.11: Plot of the allowed angles for total internal reflection inside a square microresonator as a function of index of refraction contrast between the resonator and its surroundings. Note that the first curve is the critical angle and the second curve is the 90 degree minus the critical angle. Sets of angles inside the shaded region can be totally internally reflected.

The region bounded by the θ_{crit} and 90-θ_{crit} curves contains the set of internal reflection angles capable of resulting in light ray confinement. This bounded region contains both stable resonant modes as well as unstable non-resonant modes. Depending on the reflective properties of the microcavity, the first possible mode is a 2-node 1-D oscillation between parallel walls. The second possible mode is a 4-node square path inscribed within the square resonator itself. Figure 2.12 depicts with a dashed line the fundamental 4-node inscribed square path [4, 12].

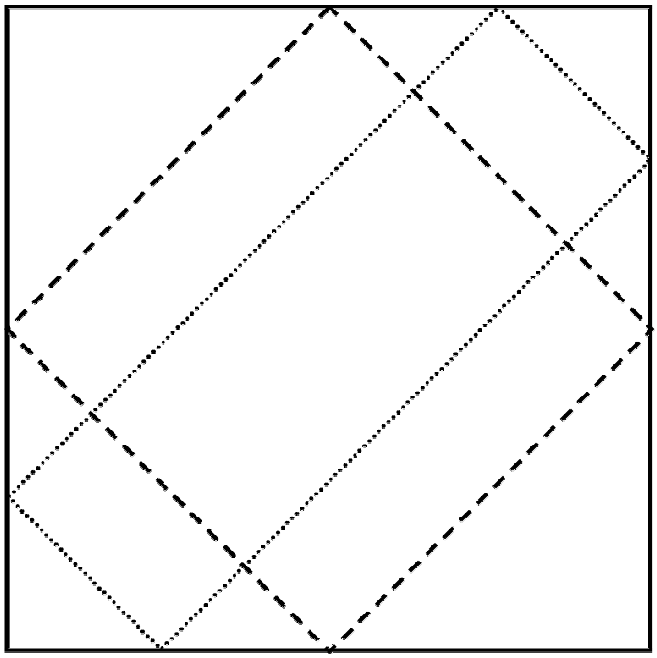

Figure 2.12: The solid lined square is the boundary of square microresonator. Inside the microresonator are the lowest loss mode, the dashed line and the lossy, related elongated rectangular modes, denoted with a dotted line.

In addition to the low loss inscribed square, a whole related family of rectangular orbits exists. Lebental, et al. have previously reported observing modes following the dotted path in Figure 2.12 with reflection points near the corners of the microcavity [4]. The path length of both the square and rectangular orbits is the same. It is possible to compute the resonant wavelengths for the dashed optical path.

$$m\lambda = n * L$$

In this equation, m is an integer reminding us that for a resonant mode to exist, the light waves traveling inside the microresonantor must be in phase. The index of the material is n, and L is the total length of a complete circuit around the optical path. L is written as:

$$L = 4 * \frac{\sqrt{2}}{2} a$$

$$m\lambda = n * 2\sqrt{2}a$$

The above equation can be used to obtain resonant frequencies for a given square microcavity geometry by iteratively changing the mode number, m. Taking the forward difference of the computed array of resonant frequencies, it is possible to solve for the modal spacing as a function of wavelength. This result is plotted in figure 2.13 for seven different edge lengths ranging from 5 μm to 100 μm.

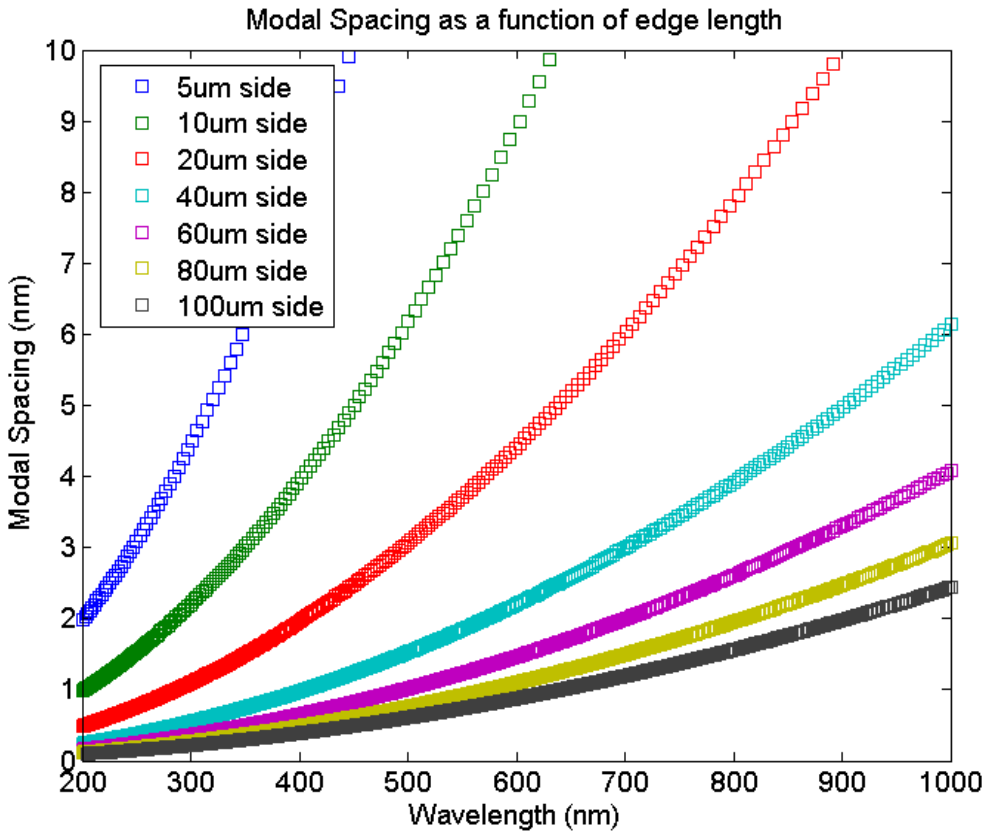

Figure 2.13: Modal spacing for squares with edge lengths ranging from 5 to 100 μm plotted over a range of wavelengths from 200 to 1000 nm.

Work has been done to extended microresonators from 2D to 3D. The most notable 3D microresonator is the microsphere. Microspheres are fabricated by heating silica fibers until spheres of molten glass form on their ends [5, 6] The microsphere is one of the few microresonators capable of supporting complex 3D mode paths.

An interesting next step in the development of 3D microresonators would be the creation of polyhedral microresonators. As seen above in the discussion of the number of modal families in a 2D microresonator, there was only a single geometry that limited the number of mode families to a single option; this geometry was a square. Making similar considerations for regular polyhedral microresonators, it is conceivable that a cubic microresonator would only support a single family of resonant modes confined on planes inside the device. These planes would resemble 2D microresonators in their mode orbits. Due to the geometry of the device, fully 3D resonant modes (i.e. a spiral) would not be possible.

The emission spectrum of a cubic microresonator is therefore expected to be a combination of the resonant frequencies of independent 2D square planes embedded in the microresonator.

Multi-Photon Lithography Background

MPL is a method for rapidly creating free-form, true 3D structures with features as small as 100 nm using highly spatially-confined polymerization initiated by the simultaneous absorption of multiple photons [9]. The photons are simultaneously absorbed by an initiator molecule, which causes the polymerization reaction. In order for

the photons to be absorbed to initiate the polymerization process, the sum of the energy of the absorbed photons must be resonant, equal to, an electronic transition in the initiator molecule. The absorbed photons may have the same energy, a state referred to as degenerate, or have different energies, referred to as non-degenerate.

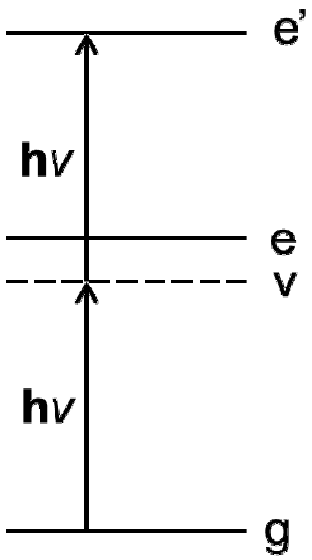

Figure 2.14: Energy level diagram for two-photon absorption.

Multi-photon absorption can be understood by examining the case of two-photon absorption (TPA). Figure 2.14 depicts the degenerate energy level diagram corresponding to TPA. Initially, a molecule exists in the ground state, until it is excited by a photon into a virtual state, v. The virtual state, v, is not an eigenstate of the molecule, but rather an intermediate state between eigenstates. A second photon must be incident on the molecule in order to excite the molecule into the energy state, e', before the virtual state decays. The probably of the transition from v to e' under ambient light is infinitesimally small; however, inside the tightly focused cone of a laser, the probability is sufficiently

high to make TPA a viable pathway to selective polymerization. TPA results in the creation of free radicals, which in turn initiates polymerization.

The rate of TPA polymerization is proportional to the square of the laser intensity. The intensity profile of the focused laser beam is not uniform. Rather, there is an inverse square relationship with respect to beam radius. The inverse square is a sharp function, where intensity drops dramatically away from the center of the beam. As a result, TPA polymerization is tightly confined in a small volume approximated by λ^3.

The specific initiator molecule and resin system used for MPL consists of the initiator, E,E-1,4-bis[4-(di-nbutylamino)styryl]-2,5-dimethoxybenzene, pictured in figure 2.15, and the acrylate monomers, pictured in figure 2.16.

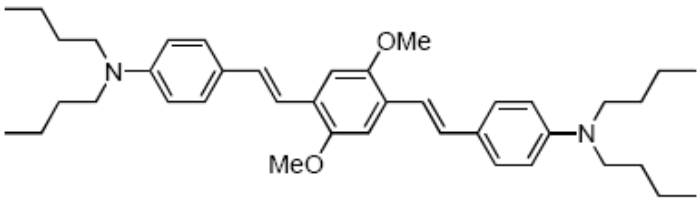

Figure 2.15: The MPL initiator molecule, E,E-1,4-bis[4-(di-nbutylamino)styryl]-2,5-dimethoxybenzene.

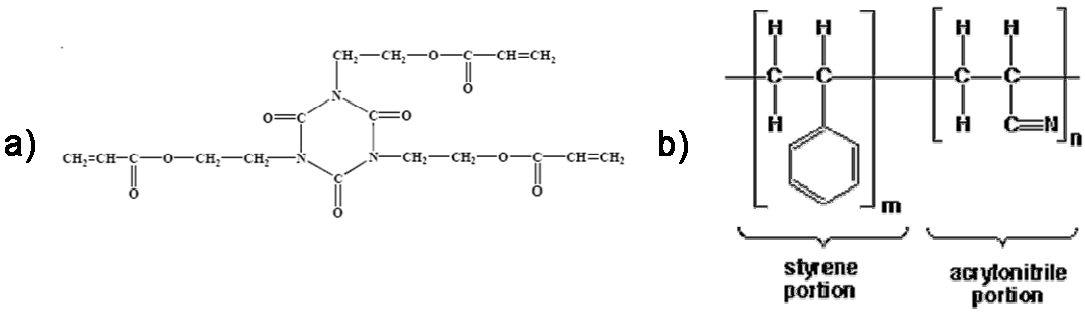

Figure 2.16: Liquid resin is comprised of two components: a) SR 9009 (50% by weight), an alkoxylated trifunctional acrylate ester and b) SR 368 (50% by weight), Tris(2-hydroxyehtyl)isocyanurate triacrylate.

As stated previously, the multi-photon absorption is highly spatially confined and only possible inside the focal volume of a laser beam. These attributes allow complex

free-form, true 3D structures to be created through the controlled translation of the laser focal volume inside the liquid resin system.

CHAPTER 3: METHODS

MPL-fabricated structures were created using a liquid cross-linkable resin of acrylate monomers. Liquid resin was first prepared by combining 50% (weight/weight) solid diacrylate monomers (proprietary, SR368, Sartomer) with 50% (weight/weight) triacrylate monomer (proprietary, SR9009, Sartomer. The combined components were heated for 10 minutes at 50 °C and stirred at 250 rpm. A spontaneous cross-linking inhibitor molecule, 4-Methoxyphenol (Aldrich) was added at 0.1wt%. The resin was then heated at 50 °C and 250 rpm for an additional 12 hours. At this time, the resin was filtered using a 1.0 μm PTFE syringe filter (Target) to remove any impurities.

A portion of the stock liquid resin solution was transferred into a new 4mL vial and a 100 mM Coumarin 481 (Exciton) solution was prepared in the resin solution. The solution was mixed at 40°C and 180 rpm for 2 hours. The multi-photon initiator, E,E-1,4-bis[4-(di-nbutylamino)styryl]-2,5-dimethoxybenzene, was added at 0.1wt% and the solution was mixed at room temperature and 180 rpm for a minimum of 6 hours. The doped resin solution is supersaturated and thus must be stored at a temperature of 30 °C to prevent the Coumarin 481 from precipitating.

In order for MPL-fabricated structures to adhere to a glass substrate, glass slides were pretreated with an adhesion promoter, 3-(Trimethoxysilyl) methacrylate (Aldrich). The adhesion promoter (5% by volume in methanol) was dripped onto the surface of the slides until the entire slide was covered. The slides were then cured on a 130°C hot plate until no liquid remained. This process was repeated two additional times.

In order to utilize the liquid resin as a source material for creating structures, the resin must be contained. A circular 50 μm thick Teflon washer was cut to fit under a 25x25 mm cover slip following the dashed lines in Figure 3.1.

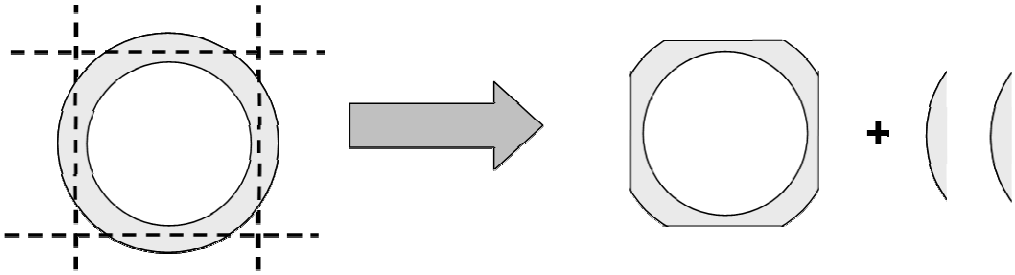

Figure 3.1: Dashed lines denote the location of cuts made to 50 μm Teflon washer in order to make it the same size as the cover slip.

The cut washer was then placed on the adhesion-promoted slide. The two semi-circular parts of the spacer were placed in the center of the slide to provide additional support for the cover slip. and resin was careful dispensed with a 1.5 inch 18 gauge needle onto the side following the pattern in figure 3.2.

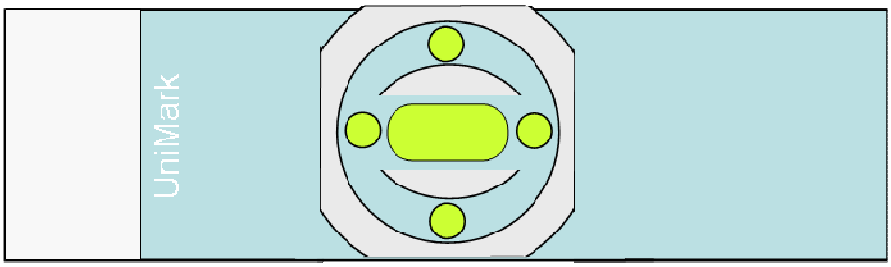

Figure 3.2: The adhesion promoted slide with the carefully placed Teflon spacer, represented as gray. The liquid resin was dispensed following the pattern of the green shapes. The two semi-circles of Teflon in the center act to maintain the thickness of the cell.

A thin 25x25 mm #0 cover slip was carefully placed over the Teflon spacer and secured on one end with tape. Care was taken to prevent trapping bubbles in the cell. In order to obtain uniform cell thickness, a folded lens tissue gripped with forceps was slowly and evenly dragged across the surface of the cover slip from taped end to opposite end. This process was repeated with a clean folded lens tissue and excess resin was wiped away. The cover slip was then secured with tape.

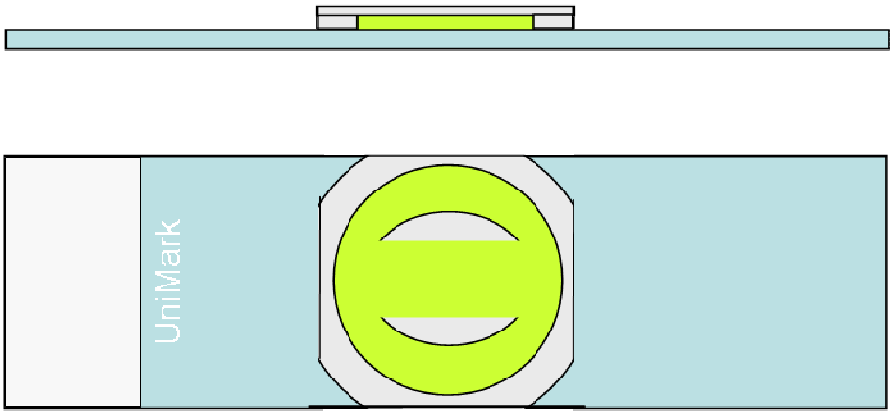

Figure 3.3: Completed liquid resin cell

The completed cell was loaded cover slip side down into the sample arm attached to the three-axis positioning system (Sutter Instruments). Care was taken to ensure that the arm was made level to the stage of the Nikon TE300 microscope. The 60x Plan APO 1.4 VC microscope objective was carefully brought into contact with the cell utilizing an index matching fluid and a fine stepper motor.

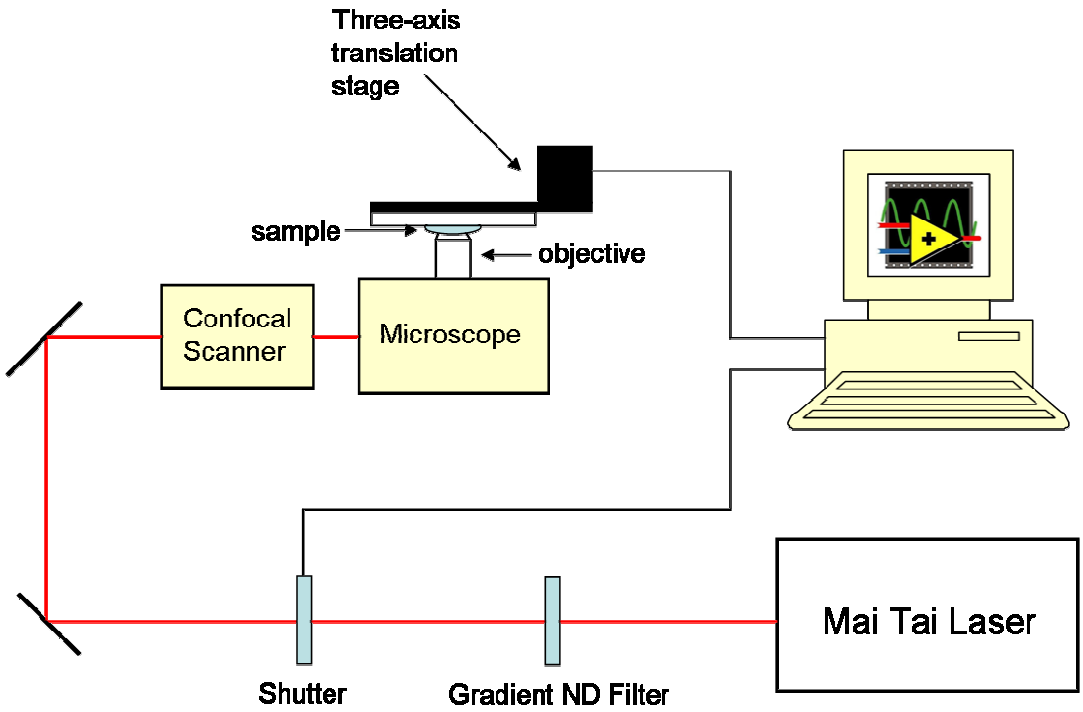

Figure 3.4: Experimental apparatus employed for MPL.

First, the location of the interface between the liquid resin and the adhesion-promoted slide needed to be found. This was done by focusing on the Teflon washer inside the resin and then translating the sample in the xy-plane until the microscope objective was located in the middle of the cell. This position was recorded in the Sutter MP-285 as (0,0,0). Using the raster beam scanner at a zoom of 1.00 and laser power of 0.70 mW (~150 μW at meter), the resin was imaged. Using knowledge of the intensity of the fluorescence as a function of position in the z (seen in figure 3.50), it is possible to reproducibly locate the interface between the liquid resin and the glass substrate. The gain on PMT1 was set to 1300 arbitrary units, a value sufficient to saturate the detector while imaging the resin. If the initial image seen was bright red, the z location was inside the resin on the high intensity fluorescence plateau. In this case, the z-position was changed in the positive direction until the sharp cutoff between the resin and slide was

found. This spatial coordinate was marked as (0,0,0). In the event that the initial image seen was not bright red, the z-position value was changed 150 μm in both positive and negative directions until the bright red was seen. The servo driven shutter was then closed utilizing the LabVIEW Virtual Instrument (VI), 3DMPL vc 3.1 developed in house by Vincent Chen.

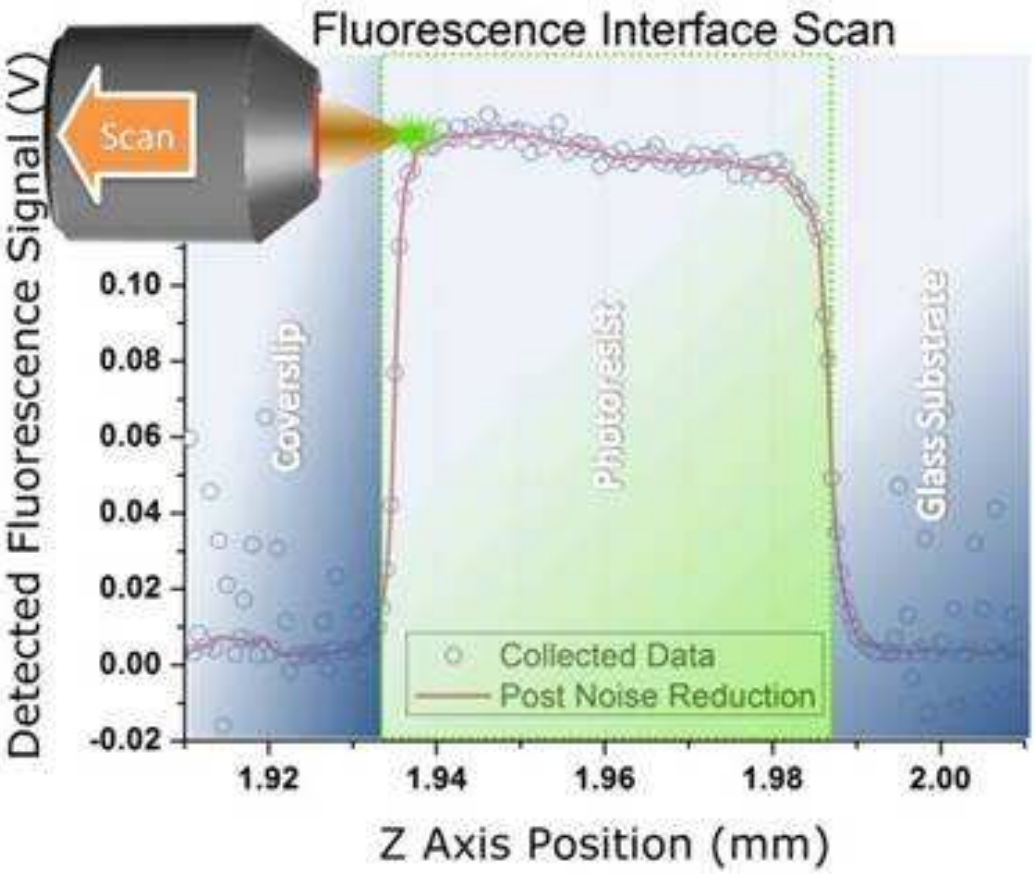

Figure 3.5: The blue regions at left and right denote the boundaries of the liquid resin cell; on left is the cover slip and on right is the glass slide. The scatter-plotted circles are fluorescence intensity recorded at different z positions, as plotted on the x-axis. The noise reduced fluorescence is plotted as a red line. Note the abrupt change in the amplitude of the red trace as a function of position. Using knowledge of this change, it is possible to reproducibly locate the interface between the liquid resin and the glass substrate. Image courtesy of Vincent W. Chen.

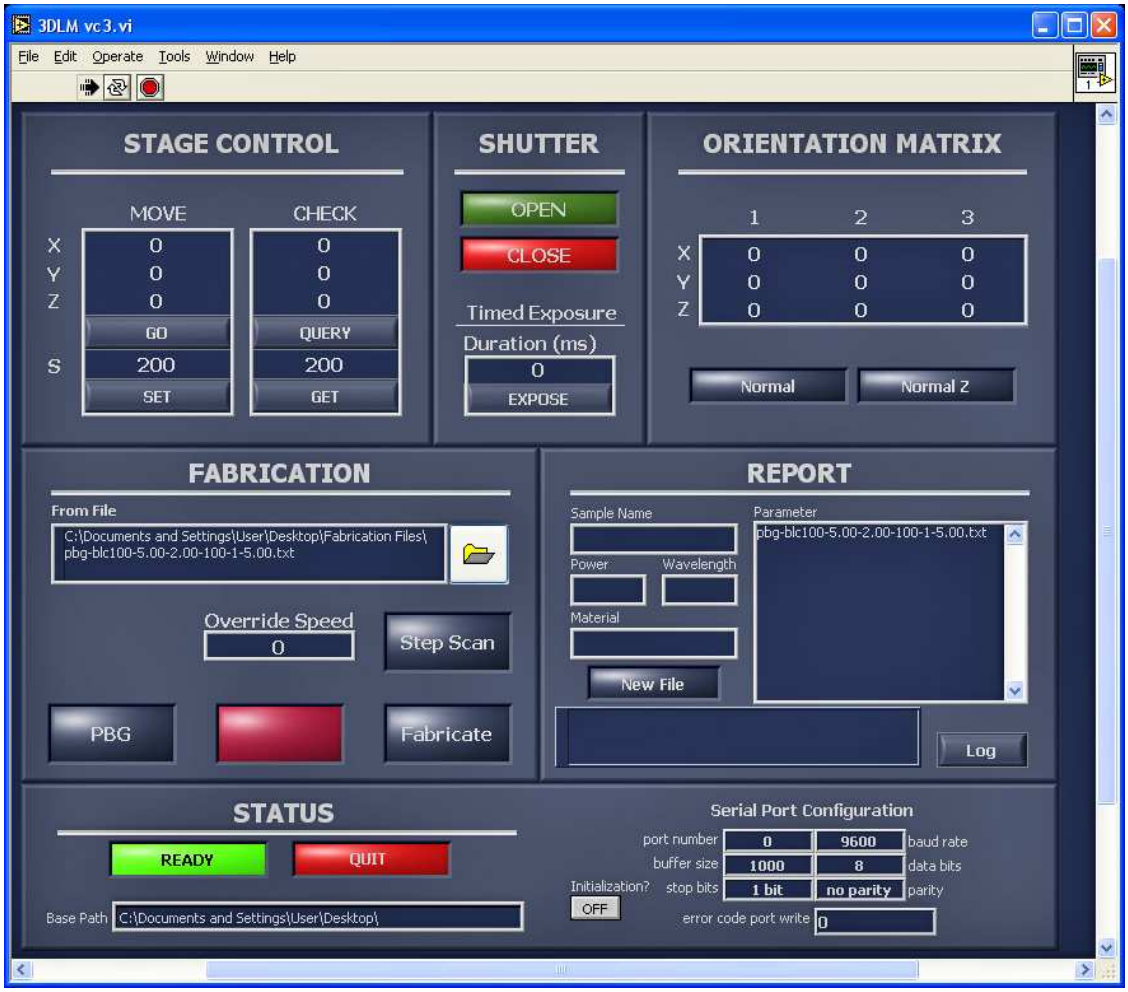

Figure 3.6: Guided User Interface (GUI) for 3DMPL.

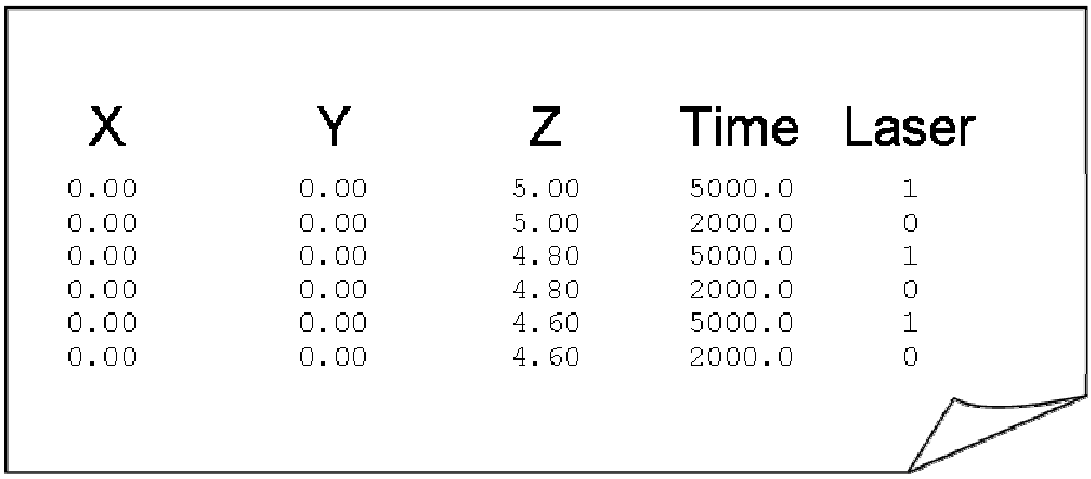

X	Y	Z	Time	Laser
0.00	0.00	5.00	5000.0	1
0.00	0.00	5.00	2000.0	0
0.00	0.00	4.80	5000.0	1
0.00	0.00	4.80	2000.0	0
0.00	0.00	4.60	5000.0	1
0.00	0.00	4.60	2000.0	0

Figure 3.7: Format of script used to create microresonators. The inputs from left to right are: x,y,z position in um, time in milliseconds and a binary value for opening and closing

the laser shutter (1 corresponds to shutter open, 0 to shutter closed). All values in the ASCII file are tab-delimited. This script can be produced with rowofblocks.m in Appendix A.

To create a 10 μm cubic microresonator elevated on a central column, the first fabricated component was the structural column. The zoom in the Bio-Rad Acquisition 3.2 software was set to 45.00, corresponding to a 3.0x3.0 micron area using a 60x objective. Next, a "user defined" box size was entered, 880x1024 lines. The default scan area is 512x512 lines in size. This scan area is not a square as would be expected, but rather forms a rectangle with an x length 15% greater than its y length. It has been empirically determined that constraining the number of lines in the x to be 86% that in the y, a true square could be created. Hence, a 512x512 scan is programmed as 440x512 and a 1024x1024 becomes a 880x1024. The ratio holds constant for squares between 40x40 and 3x3 micrometers.

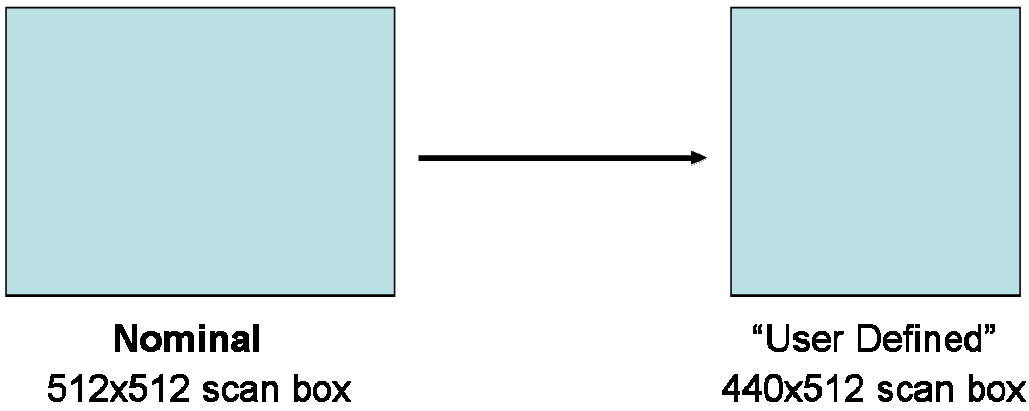

Figure 3.8: The nominal scan area of the Bio-Rad raster beam scanner produces a rectangular block, but providing a custom value for the raster scan area allows a true square to be created.

The galvomotors were engaged by clicking the red asterisk laser symbol. The laser power as measured by the power meter was 0.700 mW. The step and scan program

with a 0.2 μm step, 110224bottom0p2.txt, was loaded and executed. This took approximately 30 minutes; afterwards, the zoom in the Bio-Rad software was changed to 15.00, corresponding with a 10x10 μm box. The power was set to 0.800 mW and the step and scan program, 110224top0p2-5overlap.txt was executed. The completed structure was then examined via optical microscopy to look for defects. The process was then repeated until the desired number of microresonators was created.

Following MPL, the sample was demounted from the microscope and excess index matching fluid was removed from the liquid cell using a hexane saturated lens tissue. Tape holding the cell together was carefully removed and the cell with cover slip in place was placed in a 100% ethanol development chamber. The cell was stirred at 500 rpm for 2 minutes. The slide was subsequently transferred for two additional two-minute ethanol development stages followed by a 1.5 minute hexane bath. The slide was then dried under gentle suction provided by a fume hood.

The structures on the slide were then located with the aid of a UV lamp. The location of the structures was marked with permanent marker. Depending on the intended end use of the sample, the slide substrate was typically reduced in size to fit on a SEM mount or cut in half to isolate individual microresonators.

CHAPTER 4: INTEGRATION OF EMISSIVE SPECIES IN MICRORESONATORS

In order to introduce an emissive dye into fabricated microresonators, a selected dye was incorporated into the precursor photoactive resin for MPL, comprising acrylate monomers and initiator molecules. The emissive dye is selected to provide stimulated emission and optical gain inside the microcavity. Several criteria were developed to select candidate dyes:

1) **Emission wavelength:** As discussed above, it is desirable for a candidate dye to have a long wavelength emission maximum, in order to maximize the modal spacing of the emission spectrum. Pragmatically this means that the modulated emission spectrum from a red dye (620-750 nm) doped microresonator will be easier to resolve than one from a violet dye (380-450 nm) doped microresonator.
2) **Solubility in both the liquid acrylate monomer solution as well as the cross-linked resin following fabrication:** Based on the operational characteristics of typical dye lasers, the emissive dye should be present at concentrations of 1 mM or greater. The scientific literature contains only scare mention of dye solubility in PMMA; however, the components of the resin are highly soluble in dioxane, which is used to prepare blade casted films of resin. As a result, it is possible to utilize published dioxane solubility data as an analog for solubility in PMMA.

3) **Large Stokes Shift**: The Stokes shift is the distance in wavelength or frequency units between the absorption maximum, $\lambda_{max,\ abs,}$ of an emissive molecule and its emission maximum, $\lambda_{max,\ em}$.In order to cause fluorescence and ultimately lasing, the dye must be excited with an intense light source (i.e. a laser). This light source will be a few orders of magnitude more intense than the emitted light. Thus, if the Stokes shift is small, there is a significant chance of reabsorption of emitted light . Readsorbed light causes further emission, but because its process efficiency is less than 1, the emission is quenched.

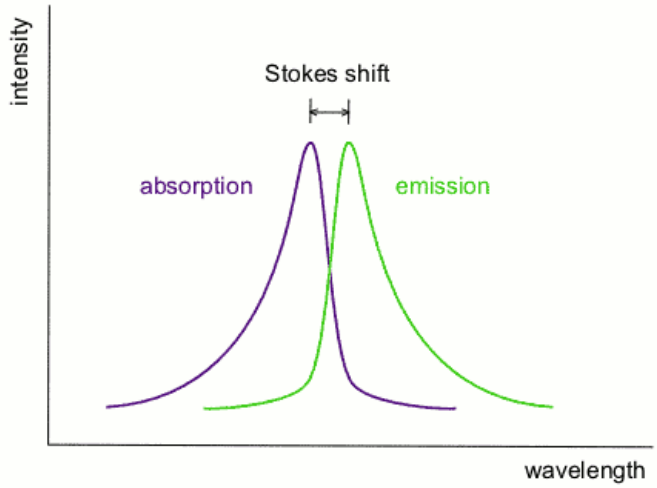

Figure 4.1: Illustrating both the absorptive and emissive curves of an organic dye. The Stokes shift is the distance between the absorption and emission maxima. Image from Wikipedia.

4) **Ability to excite dye using available light sources:** For characterization performed by our collaborators, the Zyss group, the dye must be able to be excited by their 355 nm nanosecond laser.

5) **The emissive dye is not appreciably degraded from free radicals generated during MPL nor removed from fabricated microstructures by development process** Development of structures is conducted in an ethanol bath that dissolves

non-cross-linked acrylate monomers. One criterion used to evaluate dyes was the ratio of their reported solubility in ethanol versus dioxane. It was preferred that the dye was less soluble in ethanol than dioxane, hence a ratio of 1 was desired. In hindsight, this metric may have been too arbitrary.

6) **Commercial availability at reasonable cost** It was desirable that the final candidate dyes could be obtained commercially in quantities exceeding 1 g at costs less than $100/g.

Quantum yield and photostability under long-term high-energy pumping as would occur in a laser were not considered. However, if a new dye were to be sought, these criteria would be highly desirable.

Published data on one-hundred-and-forty possible dyes were compiled into a single spreadsheet. Detailed references for all dyes can be found on the Exciton website (www.exciton.com). Initially dye selection focused on obtaining a dye with an emission peak greater than 620 nm. Several dyes with emission in this wavelength range were tested; they include DOTC Iodine, DODC Iodine, IR144 and DCM (details in table 1). All dyes unfortunately were not soluble in the solvent p-dioxane, the starting solvent for solid resin, or in the liquid resin acrylate solution.

Table 4.1: Long wavelength emission dyes tested for solubility. None were even marginally soluble in p-dioxane or the liquid resin.

Short Name	IUPAC Name	Lasing Peak	Absorption max
DOTC Iodine	(3-ethyl-2-[7-(3-ethyl-2(3H)-benzoxazolylidene)-1,3,5- heptatrienyl]-benzoxazolium iodide)	745 nm (DMSO) [13]	695 nm (DMSO) [13]
DODC Iodine	(3-ethyl-2-[5-(3-ethyl-2(3H)-benzoxazolylidene)-1,3-pentadienyl]-benzoxazolium iodide)	662 nm (DMSO) [14]	582 nm (DMSO) [14]
IR144	(2-[2-[3-[[1,3-dihydro-1,1-dimethyl-3-(3-sulfopropyl)-2H-benz[e]indol-2-ylidene]ethylidene]-2-[4-(ethoxycarbonyl)- 1-piperazinyl]-1-	871 nm (DMSO)	745 nm (DMSO)

	cyclopenten-1-yl]ethenyl]-1,1-dimethyl-3-(3-sulforpropyl)-1H-benz[e]indolium hydroxide, inner salt, compound with n,n-diethylethanamine(1:1))	[15]	[16]
DCM	([2-[2-[4-(dimethylamino)phenyl]ethenyl]-6-methyl-4H-pyran-4-ylidene]-propanedinitrile)	654 nm (DMSO) [17]	480 nm (MeOH) [18]

It became apparent that solubility would be the driving factor in selecting a suitable dye. Since scarce published data on the solubility of laser dyes in acrylate monomers exists, it was decided to compare dye solubility values for 1,4-dioxane, a solvent that readily solvates acrylate monomers. Using this criterion, 34 dyes with published solubility in 1,4-dioxane were indentified. These 34 dyes were then evaluated based on a required published solubility of the dye of at least 1 mM, a Stokes shift of >40 nm, and as long of an emission wavelength as possible. These criteria together identified 12 dyes all with emission in green-yellow. The 12 dyes were then exhaustively compared on the basis of cost, reported solubility above 1 mM, and perceived risk associated given the information at hand.

Table 4.2: The 12 most promising dyes, their emission wavelengths, solubility in dioxane, and some comments

Name	Rank	Max Lasing Wavelength	Solubility in dioxane (mM)	Remarks
Coumarin 481	1	481 [19]	20.0 [20]	High reported solubility; Quantum Yield (0.89)
Bis-MSB (1,4-bis[2-(2-methylphenyl)ethenyl]-benzen)	2	421 [21]	1.20 [22]	Promising Solubility, 70 nm stokes shift,
Coumarin 503	2	502 [23]	6.00 [24]	Similar to other Coumarins, but less data available
Coumarin 540A	2	537 (EtOH) 506 (dioxane) [24]	8.90 [25]	Due to reported solvatochromic emission wavelength shift in dioxane to 500 nm, no clear advantage over C481
POPOP	2	419 [26]	2.00 [26]	Promising solubility, stokes shift of 60 nm
Coumarin 500	3	470 [24]	5.40 [24]	Concerns over surviving

				development (reported 10x more soluble in EtOH than dioxane)
DPS	3	407 [24]	3.00 [24]	Short lasing wavelength
Exalite Series	4	350-530 [27]	1.70 [27]	Could work, but insufficient information in literature
p-Terphenyl	4	342 [28]	1.00 [28]	Lasing wavelength too short
Rhodamine 590	4	590 [29]	N/A	Poor dioxane solubility when tested in lab
Coumarin 440	4	440 [24]	only reported as EtOH/dioxane mix	Unknown solubility in pure dioxane [24]
LD 466	4	466 [30]	only reported as EtOH/dioxane mix	Unknown solubility in pure dioxane

In the end, three of the five high potential candidate dyes were members of the Coumarin dye family. Of these three, Coumarin 481 was chosen to represent all due to its very high (20 mM) reported solubility in dioxane and reported small solvatochromic shifts. The shorter wavelength, 420 nm, emitting dyes Bis-MSB and POPOP were also chosen for in-house testing due to their large Stokes shifts, 70 and 60 nm, respectively.

Solubility testing of the three dyes immediately showed that Coumarin 481 was the best candidate. It dissolved in liquid resin without stirring, was readily available in bulk at low cost, and is not prone to photodecomposition under ambient light [19].

Coumarin 481 was first synthesized in 1973 by substituting a fluorine group for a methyl group in a Coumarin with an emission peak around 430 nm. The substitution resulted in increased photostability and an emission peak of 481 nm [19]. Coumarin 481 has an absorption maximum of 390 nm in a PMMA film (figure 4.3), which agrees with reported absorption maximum in dioxane at 390 nm [31]. Experiments conducted in house have found the solubility of Coumarin 481 in the liquid resin to be at least 100 mM; two orders of magnitude larger than the typical dye concentration in a dye laser. Lastly, the index of refraction of the polymerized liquid resin with 100 mM Coumarin 481 is 1.53, a less than 3% deviation from the expected value of 1.49, based on PMMA.

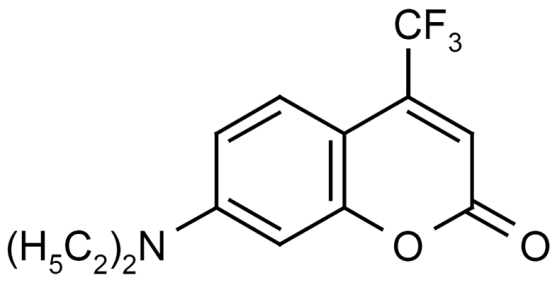

Figure 4.2: The molecular structure of Coumarin 481

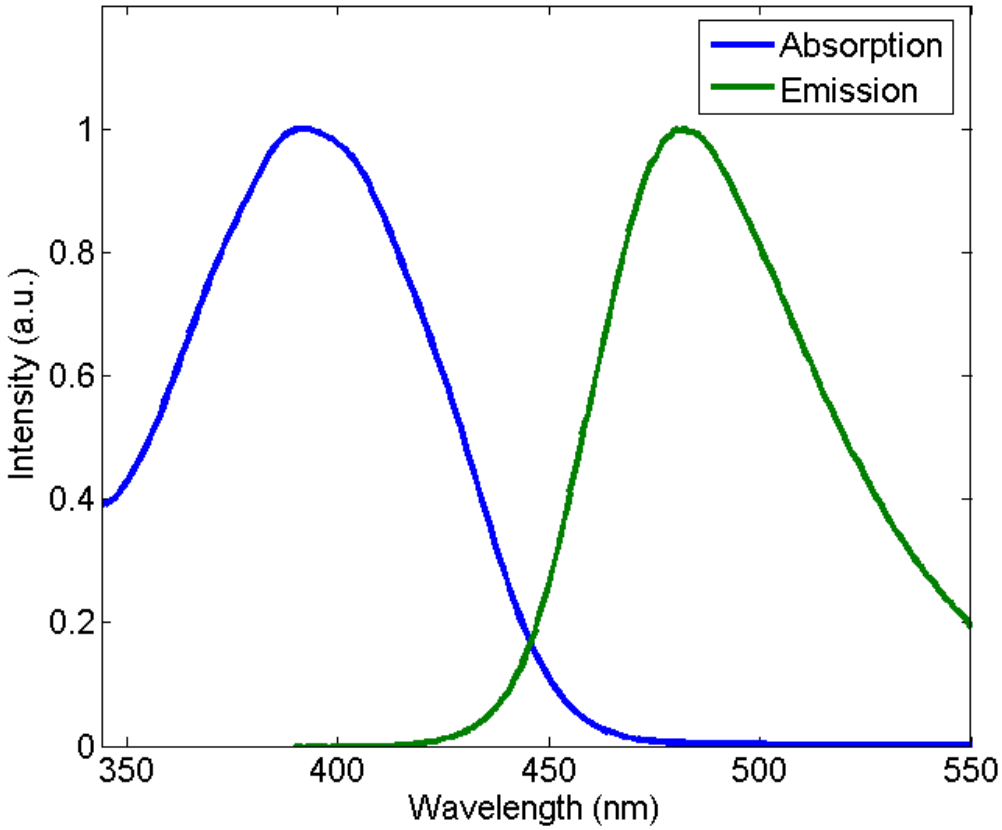

Figure 4.3: Absorbance and emission spectra from one photon polymerized PMMA films containing 10 and 100 mM, respectively . λabs,max=390 nm and λemit,max= 480 nm.

CHAPTER 5: FABRICATION

In this chapter, the MPL fabrication process is discussed along with key challenges in creating high fidelity microresonators. It is useful to provide a description of the fabrication process. To begin, an ellipsoidal focused volume of laser light is translated along a single axis to create a polymerized rod (Fig 5.1a).

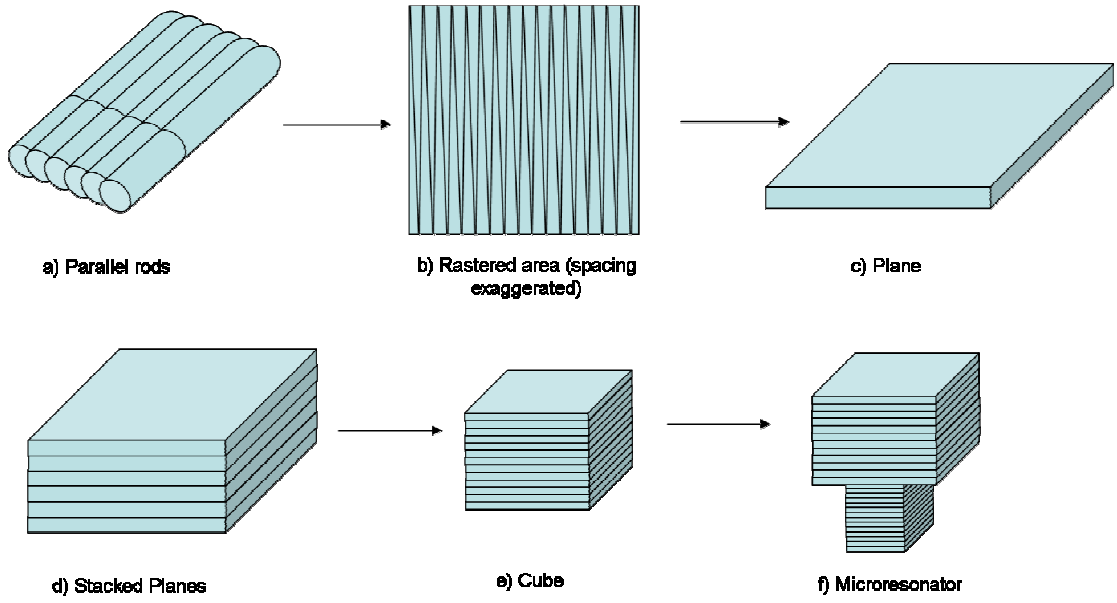

Figure 5.1: The fabrication of a microresonator from rods (a) to a scanned area (b) to a plane (c) to stacked planes (d) to a cube (e) and finally a microresonator (f).

When a predetermined line length is reached, the galvanomotors inside the raster beam scanner, reverse direction in y and change the position in x by an small increment 1(0-20 nm for a 10 μm cube or 40-80 for a 40 μm cube). The polymerized rods are not entirely parallel, but form a zig-zag pattern with small angles as seen in Fig 5.1b. As the raster beam scanner traces over a predetermined area with the laser, a plane of thickness equal to the height of the laser focal volume forms (figure 5.1c). The plane is rescanned twice per second until a mechanical shutter blocks the laser; for all microresonators in this thesis, a period of five seconds.

After completion of creating a plane of polymerized resin, the z-position of the laser focus cone is stepped a predetermined increment in the z-axis, typically 0.2 μm for smooth microresonators, via the MP-285 micropositioner. The mechanical shutter then opens and a separate plane, overlapping the preceding plane, is created (Figure 5.1d). The stacked planes eventually become cubes (figure 5.1e) and by combining cubes, a microresonator is created (5.1f).

There were three primary areas of optimization needed for creating high quality cubic optical microresonators. First, the capabilities to reproducibly fabricate microresonators to desired dimensions had to be developed. It was imperative that fabricated cubes were indeed cubes and not rectangular prisms. Second, the microresonators needed to be mechanically isolated from the fabrication substrate in order to prevent stress-relaxation-related deformations caused during. This objective also optically decoupled the microresonator from its environment, reducing potential sources of light loss. Lastly, since the smoothness of the microresonator surfaces is directly proportional to the microresonator quality factor (Q), it was critical to make the microresonators as smooth as possible.

The targeted microresonators, depicted in 5.2, all have larger cubes supported either by a central support column or four small feet. They are mechanically isolated from the substrate through the support feet or a central column. This feature acts to prevent deformation of the microresonator during development processing and is key in optical coupling the devices from the substrate. The last important feature of the intended devices are smooth surfaces.

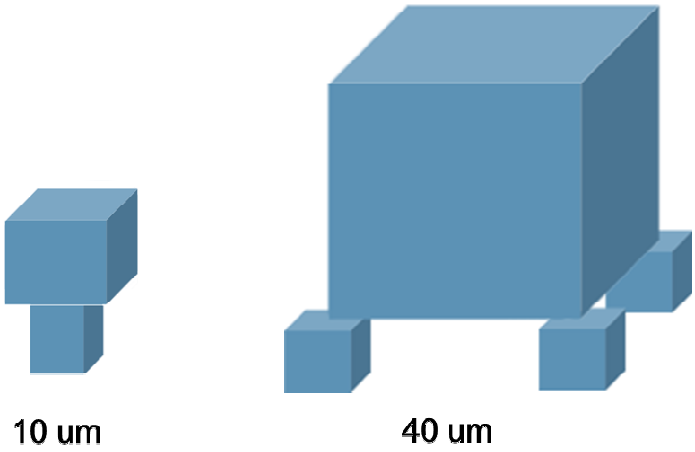

Figure 5.2: Illustrations depicting the two sizes of fabricated cubes: 10 μm, and 40 μm.

Shape Distortion

The next shape distortion issue was the appearance of sharp, upturned corners on fabricated cubes. Figure 5.3 is representative of the phenomena; it can also been seen in subsequent figure 5.5a&b. As can be seen, the top surface of the cube slopes upwards towards the edges of the cube forming a depression in the center of the microresonator. The typical deviation from a truly flat surface is 2 μm.

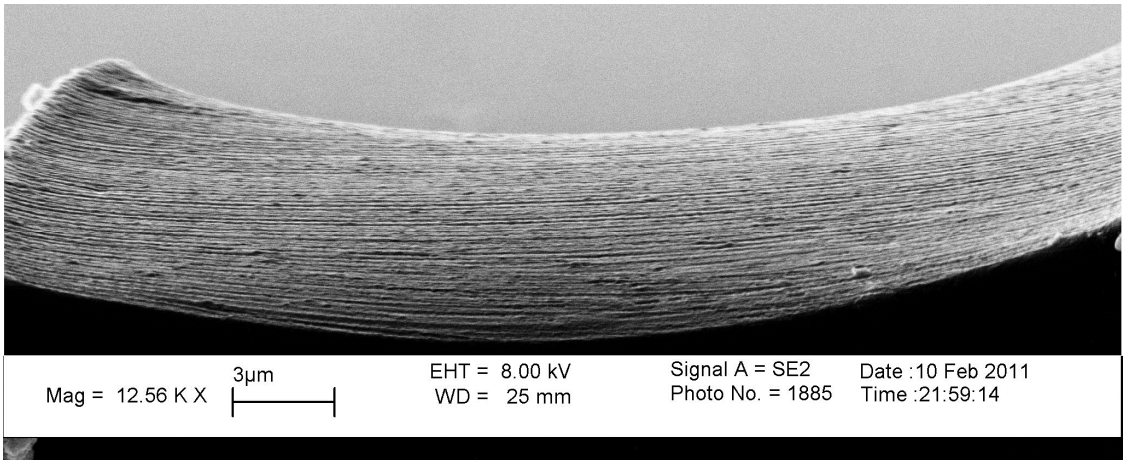

Figure 5.3: SEM image of the surface of a 40 μm cube on 10 μm cube supports. Note the upturned edges in areas of higher dosing and the central depression (Sample #110206-E: P=2.171, (z=17 (440x512)), 60x objective

During a nominal writing procedure, the Bio-Rad MRC 1024 scans 1024 lines in a single second. In order to accomplish this, the Bio-Rad MRC 1024 must change the direction of the laser beam every 1 ms. However since the galvomotors driving the laser raster scan have inertia, the change in direction is not instantaneous. Figure 5.4 depicts a model of the position (a), velocity (b) and acceleration (c) of the laser beam as it travels along a single raster-scanned line. The position of the laser can be approximated as a cubic polynomial. Using this model, it is evident that the laser spends significantly more time near the edges of the cube than it does in the center. The velocity of the laser during a single line scan can be approximated as a second-order polynomial. The acceleration of the laser during a single line scan can be approximated as a straight line. This model provides a qualitative explanation for dosing during a single line scan. It is

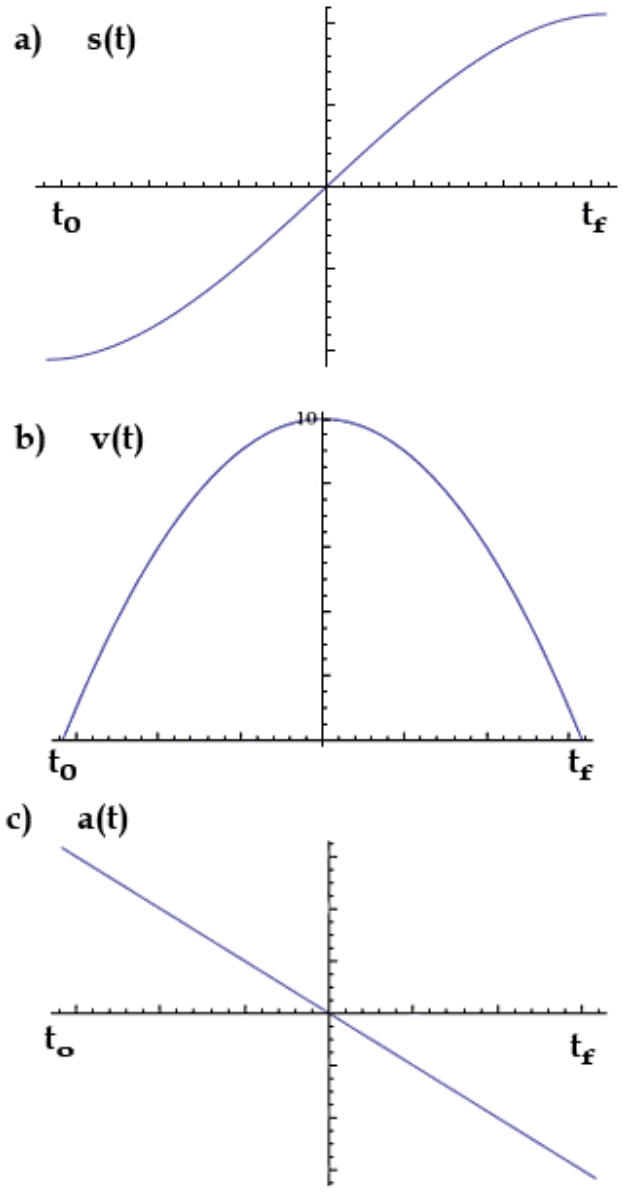

Figure 5.4: Polynomial functions representing as functions of time: a) the position of the laser focal volume, b) the velocity of the focal volume and c) the acceleration of the laser focus volume. A scan begins at time t_0 and ends at t_f.

important to remember that the next line written has been stepped in the y position, yet it still overlaps the previous line. Consequently, a single line receives twice if not many times more the dose as it received when the laser focal volume exactly traced it.

The effect of uneven dosing can be minimized by decreasing the time spent exposing each line created in the polymerized resin. There is an inverse relationship between microresonator size and raster scan speed. Thus, as the microresonator size is reduced, the raster scan speed increases. Hence, it is possible to create 10 um cubic microresonators with only minimal effects of uneven dosing. The raster scan speed can also be increased by increasing the path traveled by the laser to create a polymerized plane within the laser. This was accomplished by increasing the line density in the microresonator. Using these two relationships, it was possible to minimize the impact of uneven dosing.

Decoupling the Microresonator from the Surface

Fabricating cubes directly on the adhesion-promoted substrate results in the creation of distorted structures. Figure 5.5 shows the volume distortion typical in two cubes fabricated directly on the substrate. The difference in edge length at the base and top of both cubes is ~20%, a non-trivial value. This kind of distortion has been attributed to shrinkage of the microstructures resulting from both shrinkage during the fabrication process as well as the out diffusion of unreacted mass during sample development.

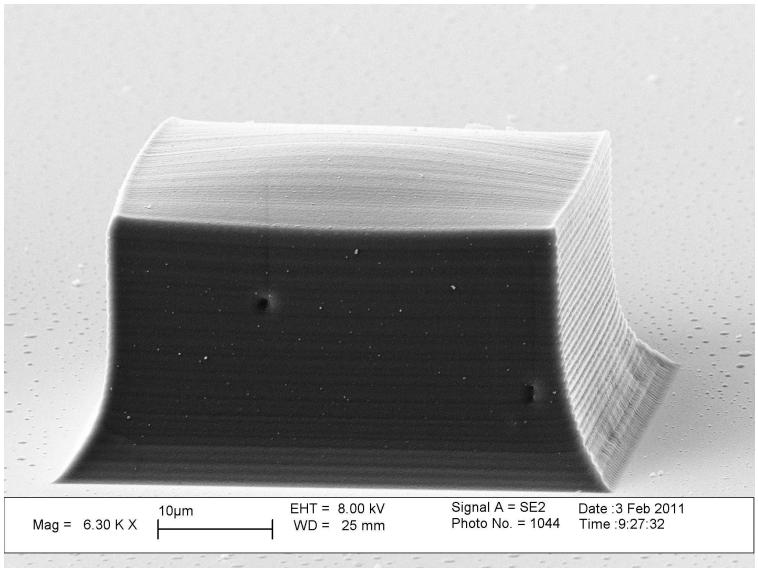

Figure 5.5: a 50x40 µm rectangular block showing a tapering resulting from shrinkage (110202-IV: 0 mM Coumarin 481, 60x objective, P=2.499 mW (z=4.46 (512x512))

The tapered shape of the cube can be explained in terms of deformable body mechanics. Figure 5.6 depicts the intended shape of the cube via a dashed line. The intended and actual volumes of the cube are nearly identical immediately following fabrication. The fabrication process mechanically bonds the cube directly to the rigid, higher Young's modulus glass substrate. During development, diffusion of unreacted mass occurs isotropically on the boundaries of the cube. As a result the cube seeks to uniformly contract to an equilibrium shape of the same geometry. This is possible within the equilibrium zone of the cube, away from the fixed boundary of the substrate., Between the equilibrium region and the substrate exists a transition region of tapered faces on the cube.

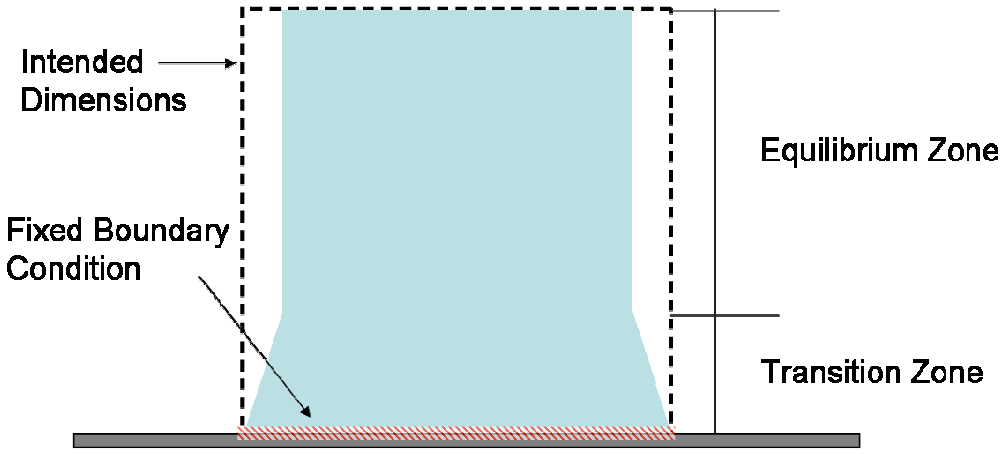

Figure 5.6: A deformed cube following development. Note that the morphology of the cube may be divided into two regions, an equilibrium region and a transition zone. The equilibrium zone has uniformly stress relaxed and retains rectilinear characteristics. The transition zone has a tapered shape following the stress distribution in the cube.

This mode of distortion can be nearly eliminated by mechanically isolating the cube from the substrate. This is seen in figures 5.12,

Surface Roughness

The magnitude of the surface roughness for a microresonator is inversely proportional to the quality factor (Q) of that device. The impact of this reduction in Q can be considered in the three emission peaks, each representing a resonant wavelength, shown in figure 5.7. Starting on left, it is possible to see that the broadest, shortest peaks are observed in the roughest microresonators with low Q. As the roughness of the microresonator is reduced, the Q increases and the emission peaks narrow and increase in intensity.

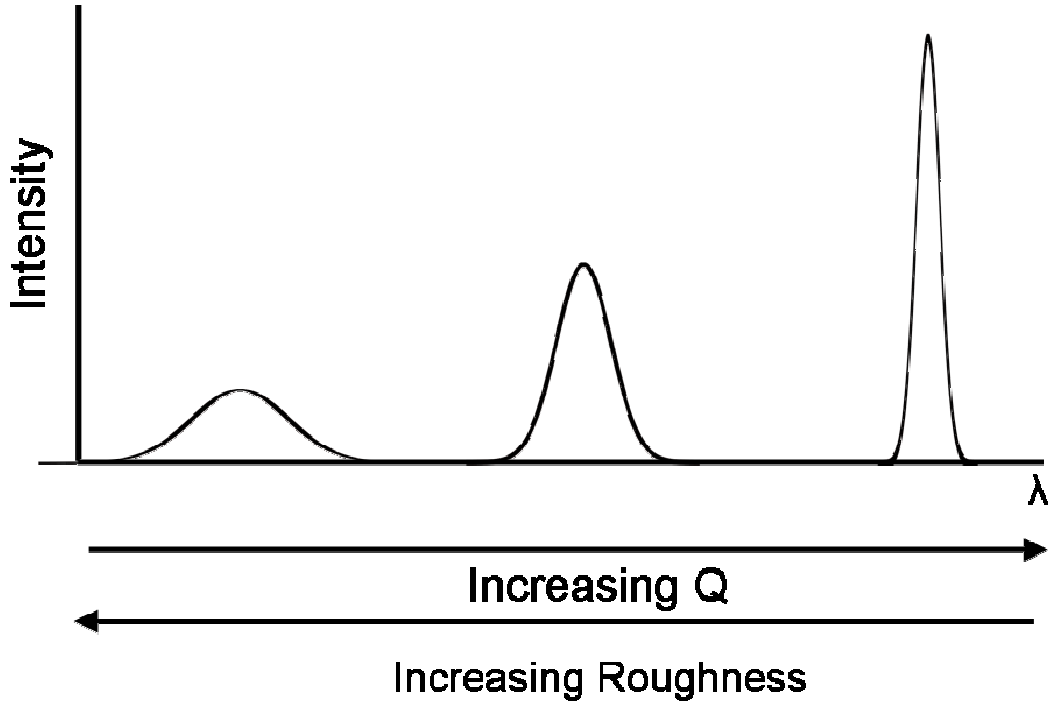

Figure 5.7: depicting the inverse relationship between Q and surface roughness. Note that high Q values with sharp, intense peaks are the most desirable outcome.

In this discussion of surface "roughness" it is important to remember that the primary phenomenon of concern is undesirable periodic surface modulation and not random roughness, which exists, but at a smaller scale. Thus all discussed mechanisms causing "roughness" can be controlled through tweaking the fabrication parameters.

The first mechanism to be considered is the consequence of polymerizing the liquid resin while translating the z-axis. The resulting structure, seen in Figure 5.8, closely resembles the outline of an accordion's bellows.

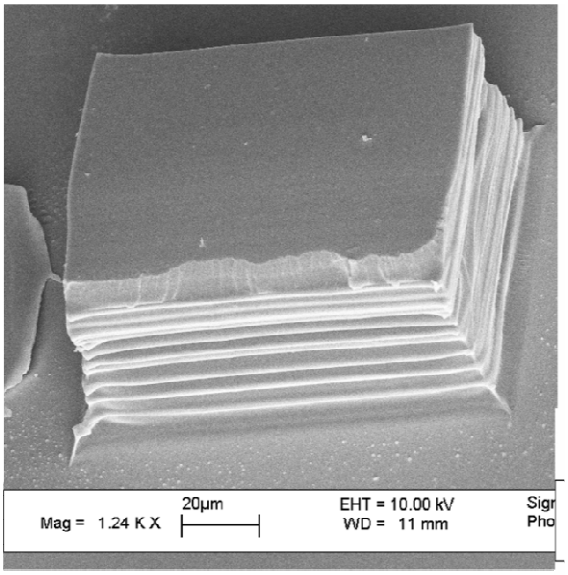

Figure 5.8: SEM image of a ~100x100 µm block fabricated via continues writing during translation. Note the rough surfaces resulting from the interaction of the z-translation and the raster scan. Fabrication parameters: 0 mM Coumarin 481, 40x objective, P=3.51 mW, (z=2.75 (512x512))

This morphology can be minimized, but not eliminated even while translating at very small z-translation speeds. Figure 5.9 schematically depicts that during the entire interval of t1 to t2, the laser excites the resin while the z-position is continuously in motion. Noting that this z-translation occurs simultaneously with the xy motion of the raster scan helps explain the aforementioned accordion morphology.

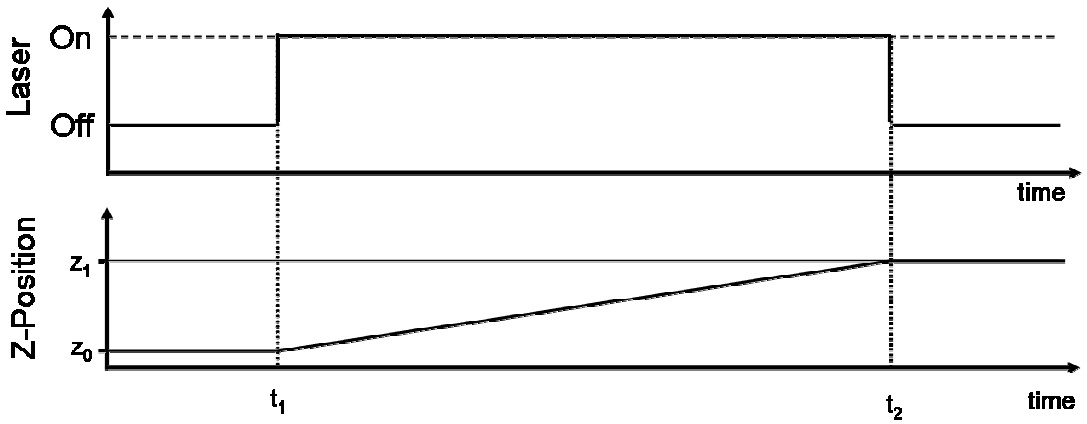

Figure 5.9: The relationship between laser exposure and z-translation as a function of time for continuous writing.

By considering the volume of resin scanned by the Bio-Rad confocal device, as planes of non-negligible thickness, it was logical to consider structures consisting of simple stacked layers. This method dubbed "Step and Scan" synchronizes the opening of a mechanical shutter with z translational steps. Figure 5.10 shows that laser exposure times (t1→ t2 and t3→t4) occur only when the z-position is constant. It is only before, between and after these intervals that the z-position is changed. This process eliminates the zig-zag morphology seen previously.

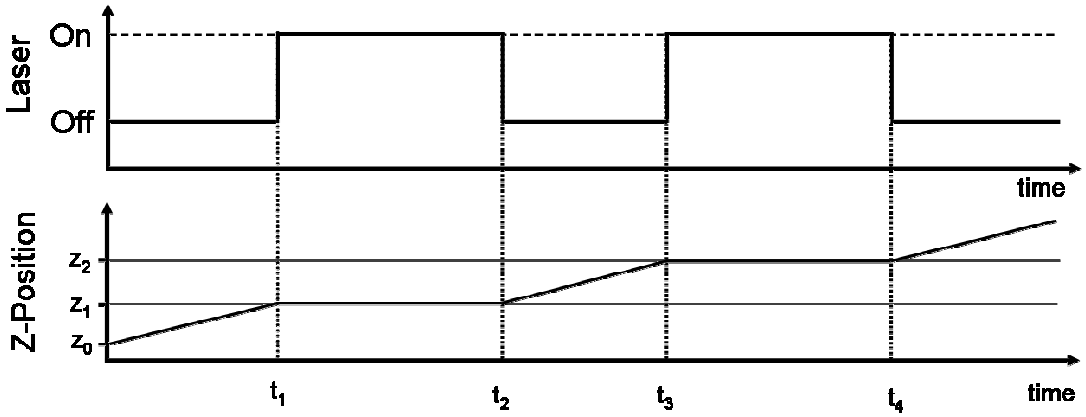

Figure 5.10: The relationship between laser exposure and z-translation as a function of time for "step and scan."

The success of this methodology is shown in figure 5.11. It displays a well-formed 40 μm cube with a layer spacing of 1.0 μm. The overall shape of the structure matches the target structure, a cube, and the sides are significantly smoother than the example in 5.8.

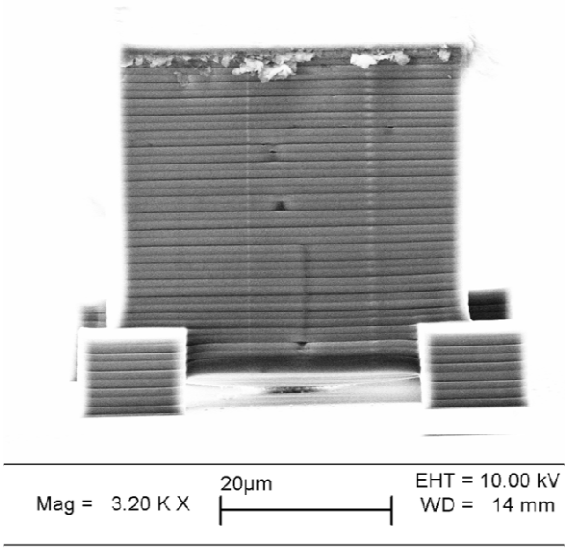

Figure 5.11. SEM Image of a 40x40x40 µm cube with low overall shape distortion. Note the prominent 1.0 µm layer spacing. Fabrication parameters: 100 mM Coumarin 481, 60x objective, Pfeet=1.11 mW (z=15 (440x512)), Pcube=1.50 mW (z=4.46 (440x512)).

Transitioning from a continuous writing procedure to "step and scan" caused significant improvements in microresonator morphology as well as reduced side wall roughness, but additional optimization was necessary. The prominent layering seen in Figure 5.11 has a period of 1 µm and was not deemed to be sufficiently smooth enough to give rise to a high quality factor.

An expedient method to reduce the side wall surface roughness of the microresonator is to change the size of the z-step taken when writing different planes of polymerized material. Figure 5.12 depicts five different z plane step increments ranging from 0.20 µm to 3.0 µm. In the 2.0 and 3.0 µm z step increments, the inter-plane spacing is regular and the modulation of the surface is on the order of 10^2 nanometers. Although it is difficult to see the differences in surface modulation between the 0.20, 0.50 and 1.0 µm z increments in these images, the 0.20 µm has the smallest surface modulation, on the

order of 10^1 nanometers. From these experiments, it became clear that a spacing of 0.20 μm produced the smoothest sides.

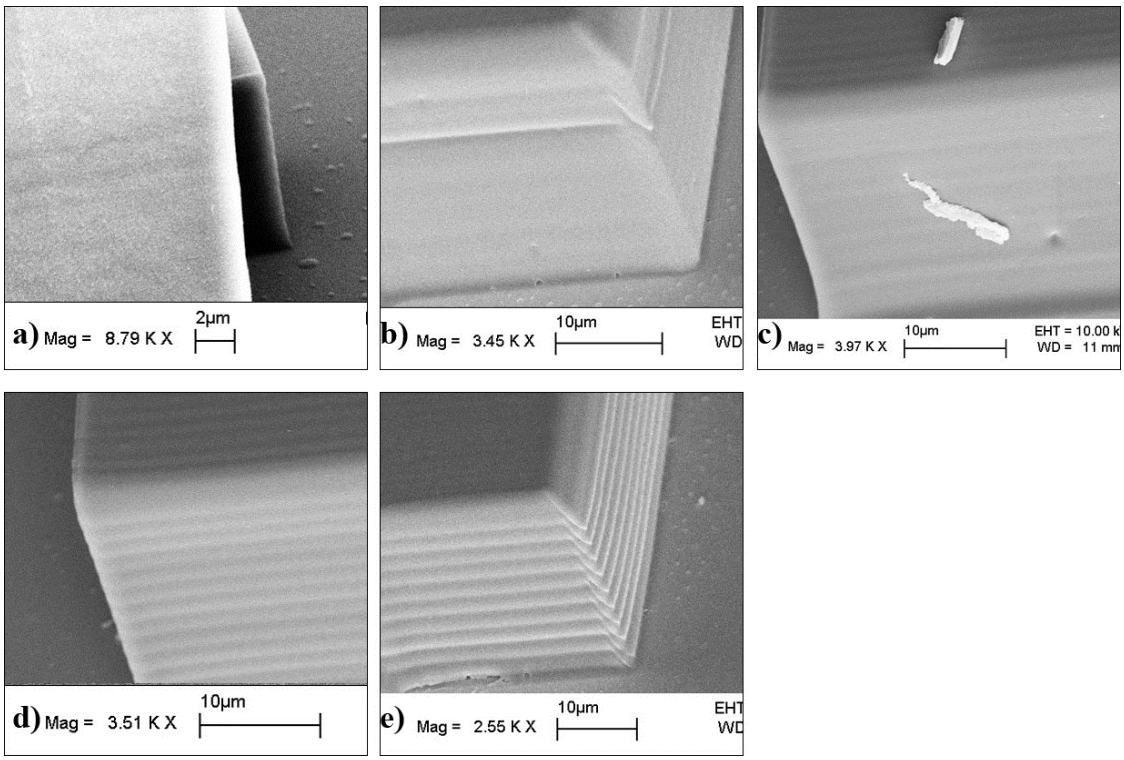

Figure 5.12: SEM images of MPL–fabricated blocks with different z plane spacings: a) 0.20 μm b) 0.50 μm c) 1.00 μm d) 2.00 μm and e) 3.00 μm. Parameters for block a: 100 mM Coumarin 481. Additional parameters: P_{feet}=1.113 mW (440x512), P_{cube}=1.299 mW (440x512), 60x objective. Parameters for blocks b-e: 0 mM Coumarin 481, P=3.06 mW (z=2.75 (512x512)), 40x objective. Created via script: LinespacingTest.m

Once the side wall roughness was well characterized, it became necessary to address the top surface roughness. Top roughness arises from the periodicity of a tightly-spaced raster scanned area, where individual line segments form the total raster scanned area. The Bio-Rad MRC 1024 confocal scan head has four different primary "box sizes", control over the number of lines in a given box, plus the ability to create custom "box

sizes." The four primary options are box sizes of 128x128, 256x256, 512x512 or 1024x1024 lines. It is possible to scan the same fixed area with differing line densities.

Figure 5.13 illustrates four different line densities, (a) 3.2 lines/μm, (b) 6.4 lines/μm, (c) 12.8 lines/μm, and (d) 25.6 lines/μm. The lowest line density forms a block with wide, periodic major bands every 1.4 μm. Increasing the line density from 3.2 lines/μm to 6.4 lines/μm reduces the predominance of major bands, and the top surface appears as only entirely the product of smaller lines.

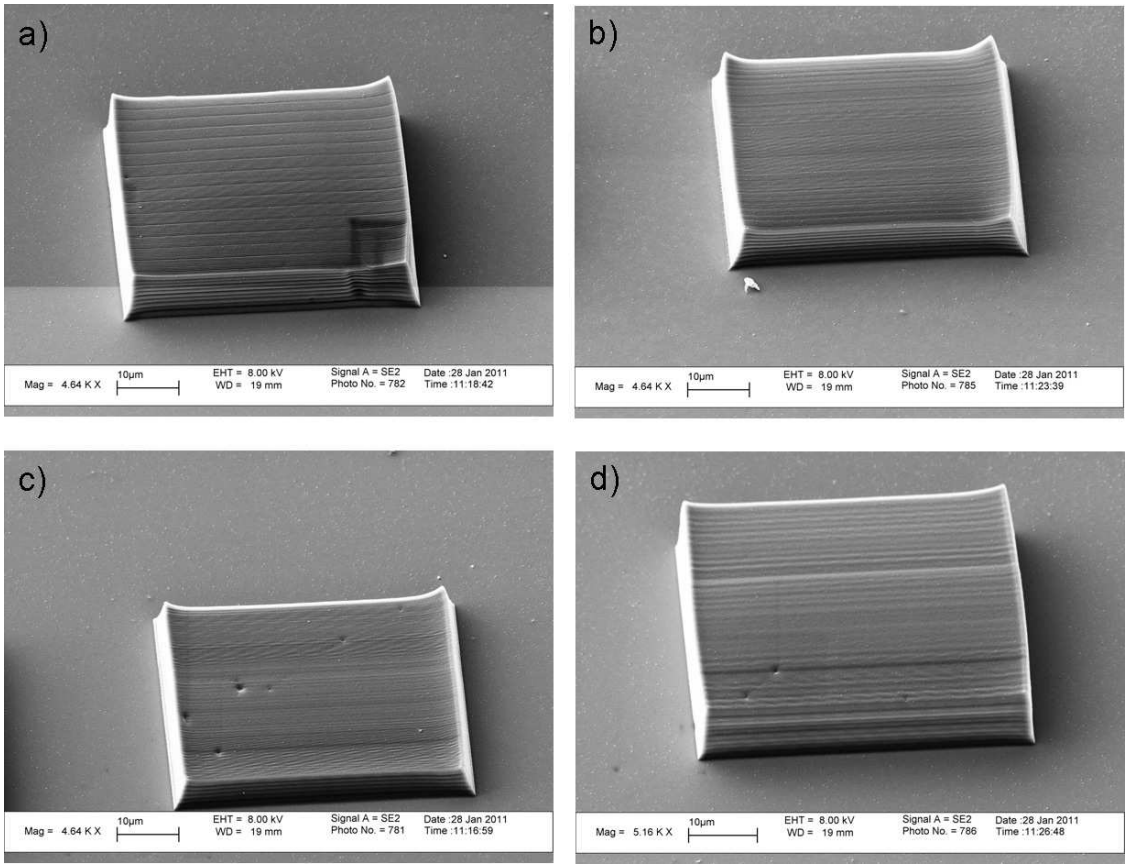

Figure 5.13: SEM images of four 40x46x8 μm blocks created with variable line density a) 128x128 (3.2 lines/μm) (Note: SEM damage in lower right corner) b) 256x256 (6.4 lines/μm) c) 512x512 (12.8 lines/μm) and d) 1024x1024 lines (25.6 lines/μm).

There are a few difficulties associated with determining quantitatively the top line spacing and height of the protruding lines. The first measurement attempts were made with Scanning Electron Microscopy (SEM). The technique proved useful to get an overall image of the top surface, but the features on top of the microresonator possess soft edges that make fine focusing above 6 kx difficult. This is compounded by the fact that the electron beam causes the microresonator to deform even at accelerating voltages as low as 3.0 kV. As a result, SEM is helpful, but cannot provide quantitative measurements for roughness.

Another useful instrument for measuring surfaces with micrometer scale roughness is the Atomic Force Microscope (AFM). The AFM utilizes a cantilevered probe to interrogate a surface either by dragging the probe over the surface (contact mode) or oscillating the probe at its resonant frequency to only intermittently touch the surface (tapping mode) [32].

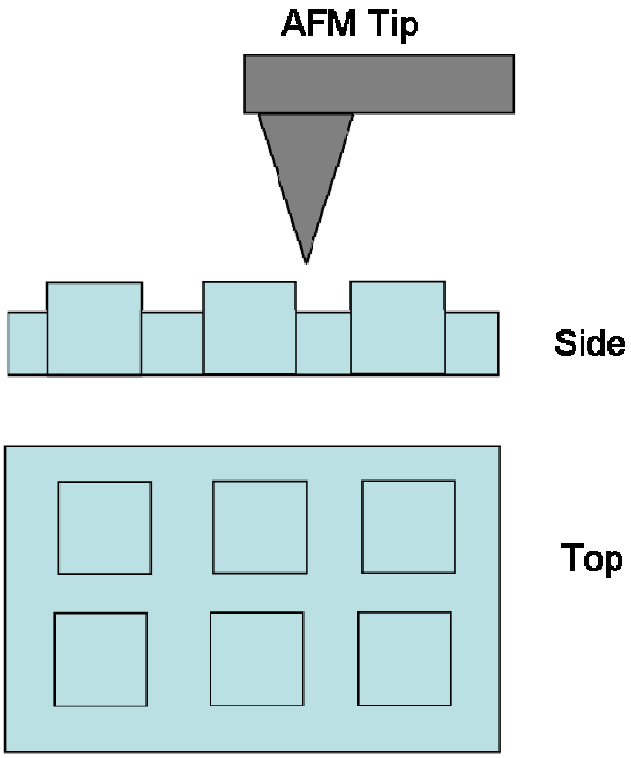

Figure 5.14: AFM tip scanning a representative area of 10 μm cubes embedded in a larger 7 μm thick polymerized block.

It was possible to conduct AFM measurements in tapping mode on the top surfaces of 10 μm cubes embedded in a 7 μm block of polymerized resin (depicted in figure F); however significantly different moduli of the rugged etched silicon cantilever tip and the soft resin made it challenging to apply sufficient force to properly image without destroying the sample. Figure 5.15 shows the top surface roughness on a 10 cube; of note is the large hole created by the AFM tip along the bottom of the frame. Impalement can also be confirmed independently by comparing the natural frequency of the cantilever before and after measurement.

Positioning the cantilever on the sample was challenging. The 35 μm wide cantilever needed to have its 10 μm long tip placed on the 10x10 μm square using a 4x magnification camera. The cantilever tip had to image a large area containing the

samples by detecting the increase in height between the embedded cubes and their host matrix. More than once, this process resulted in the creation of a double tip, necessitating the use of a new tip.

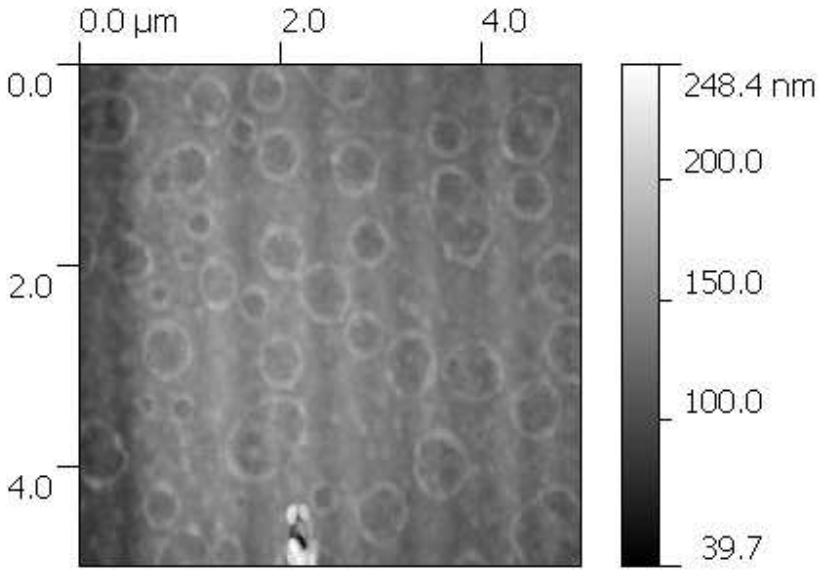

Figure 5.15: AFM image of a 5x5 µm area on top of a 10 µm square with 440x512 box size (51.2 lines/µm). The vertical bands are the expected result of the fabrication process. The large dark spot on the bottom of the sample is a result of impalement by the AFM tip. The one unexpected result of the data collection was the discovery of numerous craters on the surface of the square.

Figure 5.15 shows a 5x5 µm area on top of a 10 µm square with 440x512 box size (51.2 lines/µm). The vertical bands are the expected result of the fabrication process. The large dark spot on the bottom of the sample is a result of impalement by the AFM tip. A surprising result of AFM was the discovery of numerous surface craters roughly 0.5 µm in diameter and typically 20 nm deep from rim to bottom. These craters are likely the result of solvent evaporation during sample development. This phenomenon has been coined “the coffee ring effect” after the ring left by a coffee cup on a surface [33, 34].

A rapid, “just-as-good” alternative to AFM is optical profilometry. Optical profilometry is a non-contact method for measuring surface roughness using light to

resolve surface features down to λ/20. Using the LEXT laser 3D confocal optical profilometer (Olympus), it was possible to rapidly image several 10 μm cubes embedded in a 7 μm matrix. Figure 5.16 shows three 10 μm squares with varying line densities. Each scan was acquired in under a minute compared to over an hour on AFM.

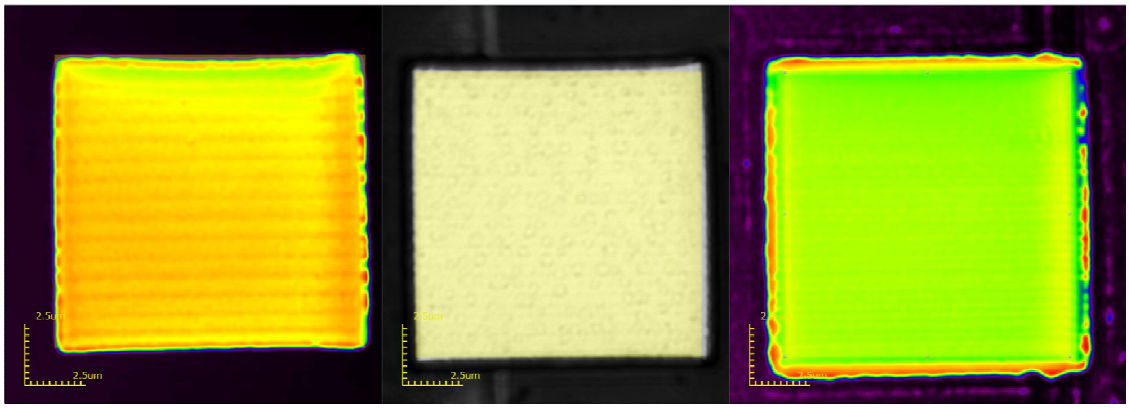

Figure 5.16: Surface topography imaged via optical profilometry. All squares are ~10x μm on an edge. From left to right, 220x256 box (25.6 lines/μm), 440x512 (51.2 lines/μm) and 880x1024 (102.4 lines/μm).

The surface roughness of the three line densities were quantified with the LEXT 3D software. The root mean square surface deviation was chosen as the figure of merit for comparing the roughness of the top surfaces. At the lowest line density, 25.6 lines/μm, the RMS surface deviation was 0.252 um. The RMS value more than halved by doubling the line density to 51.2 lines/μm. Finally, at the highest line density, 102.4 lines/μm, the RMS surface deviation was only 0.075 um. This represents a 70% reduction in RMS surface deviation and clearly demonstrates that higher line densities are desirable for reduced RMS surface deviation.

Table 5.1: The root mean square (RMS) surface deviation of three different raster line densities. Note that the RMS deviation decreases with increasing line density.

Raster Line Density	RMS Surface Deviation (um)
220x256 (25.6 lines/μm)	0.252

440x512 (51.2 lines/μm)	0.122
880x1024 (102.4 lines/μm)	0.075

Discussion of fabricated devices

Cubic microresonators with edge lengths of 10 μm and 40 μm were successfully fabricated. After fabrication and development the devices were examined via scanning electron microscopy (LEO GEMINI 1530 and 1550, Carl Zeiss, Germany). Images were collected with the SE2 secondary electron detector to enhance contrast.

The first generation of microresonators was intended to demonstrate the ability to create a supported cantilever structure resembling a table. Figure 5.18 shows the first successful microresonator table fabricated on left with a comparison to the intended dimensions on right. The tolerance on these features ranged from 4% to 30%. The primary tolerance concern was the overall edge length of “table top;” it deviated 15% from intended. This deviation was eliminated in subsequent generations of microresonators as discussed in the shape distortion section of this chapter.

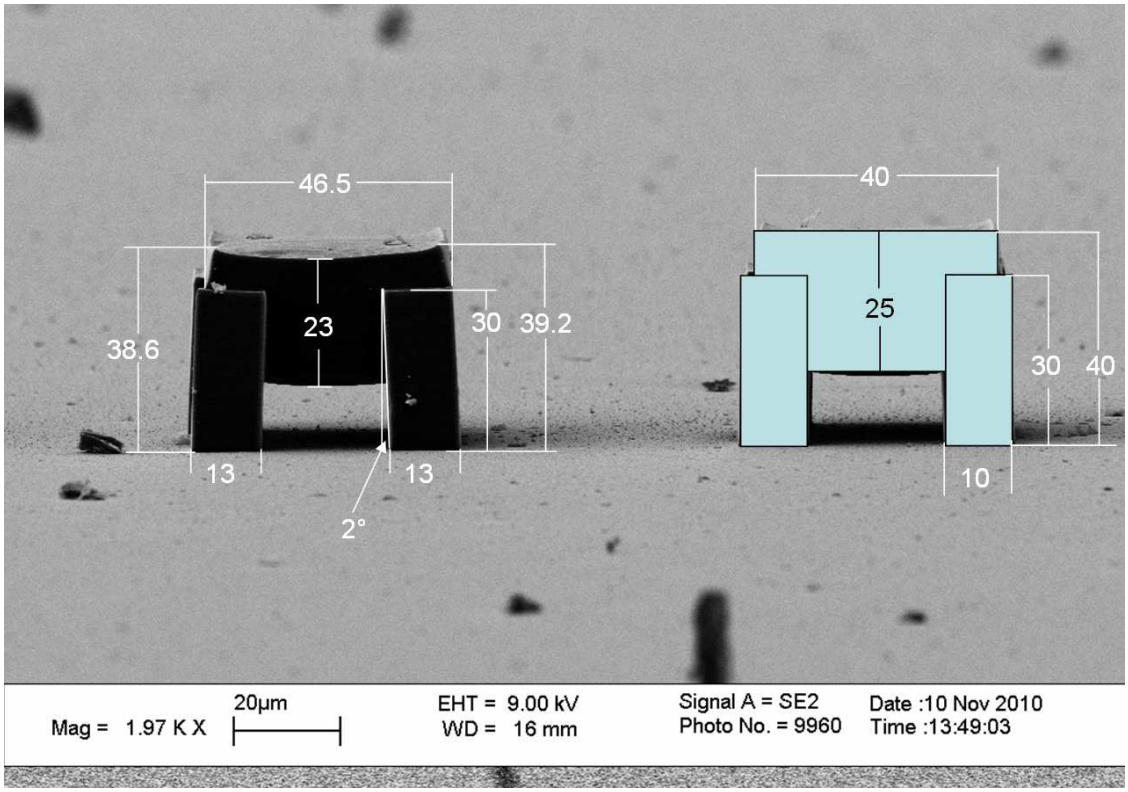

Figure 5.17: SEM image of first generation "micro-table." On left, a fabricated micro-"table" with tolerances of 4 to 30% with respect to intended dimensions. On right, a drawing representing the intended fabrication dimensions. P_{feet}=1.40 mW (z=15 (512x512)), P_{cube}=1.60 (z=4.46 (512x512)), 40x objective.

In comparison to the first generation devices in figure 5.17, the second generation of cubes, seen in Figure 5.18, more closely matched their intended dimensions. The intended dimensions were 40x40x40 μm cubes supported by 10x10x10 μm feet. Most crucially, the edge length of the cubes only deviated 2-6% from their intended length of 40 μm.

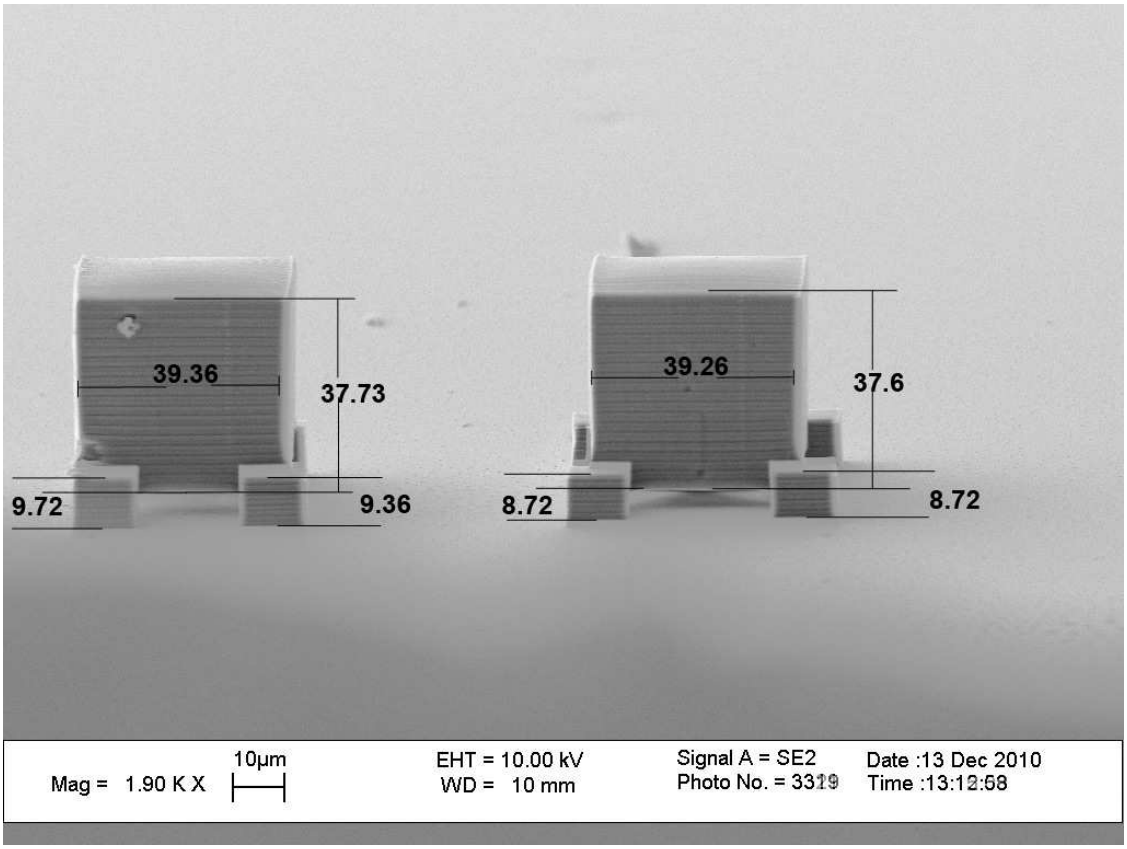

Figure 5.18: SEM Image showing the side elevation of two 40 µm cubic microresonators with 1.0 µm spacing. Fabrication parameters: 100 mM Coumarin 481, 60x objective, Pfeet=1.11 mW (z=15 (440x512)), Pcube=1.50 mW (z=4.46 (440x512)).

Examining the same two microresonators from above (note: that the left cube in Figure 5.17 is on right in Figure 5.18 and vice versa) reveals that the main cubes were fabricated with a high degree of accuracy. The width and depth of the left cube are within 0.1% (60 nm) each of other; while the right cube has edge lengths within 0.4% (120 nm). It is difficult to compare the measurements previously taken in Figure 5.18 with those in Figure 5.19 due to the different angles of observation. Despite this, the overall fabrication of the cube is satisfactory. There is only one minor issue, the placement of supporting feet with respect to the cube.

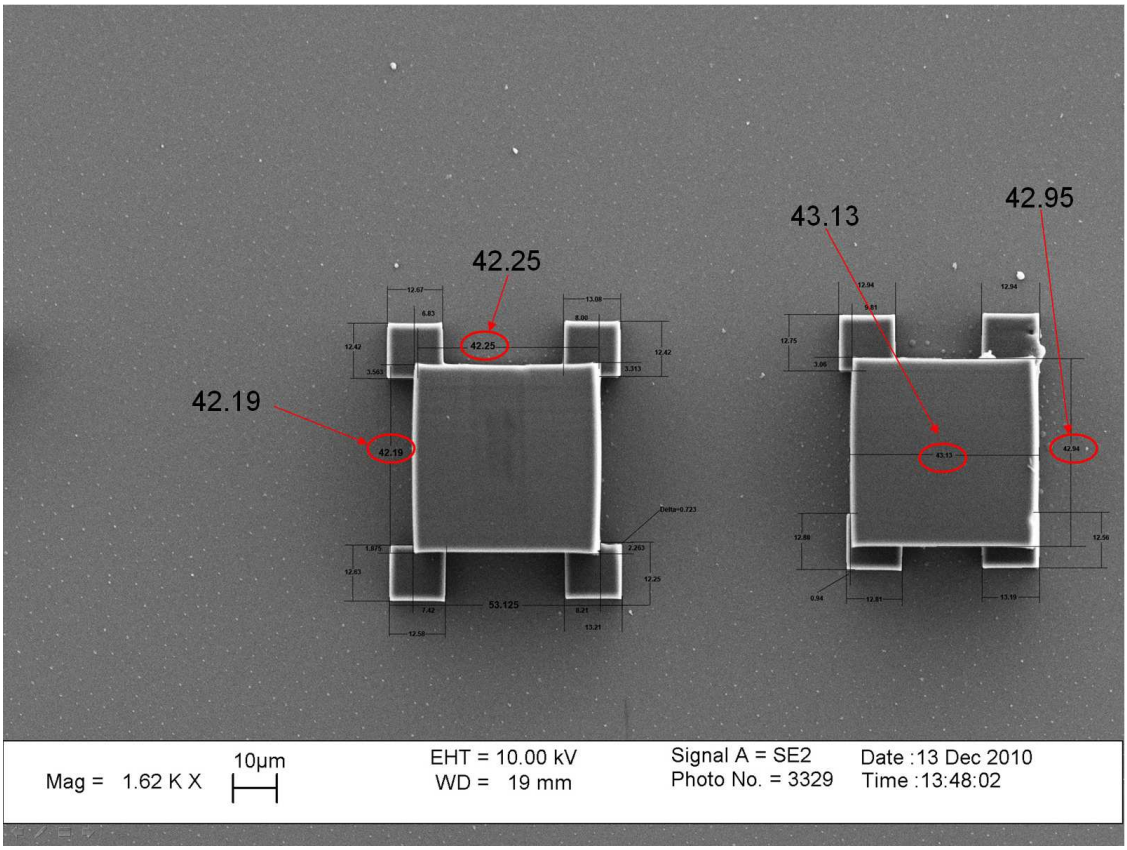

Figure 5.19: SEM image of Overhead view of cubes in figure 5.19. Note that in this image, the cube position is reversed from previous image, 5.19; the cube on the right in figure A is on the left in figure B. Fabrication parameters: 100 mM Coumarin 481, 60x objective, Pfeet=1.11 mW (z=15 (440x512)), Pcube=1.50 mW (z=4.46 (440x512)).

The next generation of 40 µm cubic microresonators reduced the z-spacing from 1.0 µm to 0.2 µm. The 1.0 µm spacing of the cubes in figure 5.18 is readily apparent like a washboard. In comparison, the 0.2 µm walls in Figure 5.20 require close examination to find small differences between the fabricated layers. Unfortunately, in order to obtain improved surface smoothness, the cumulative dose received by the resin needed to be increased. It was not possible to find an optimal dose for 40 µm cubes with a 0.2 µm spacing and all fabricated cubes had smooth regions like Figure D as well as a large void as seen in Figure 5.21.

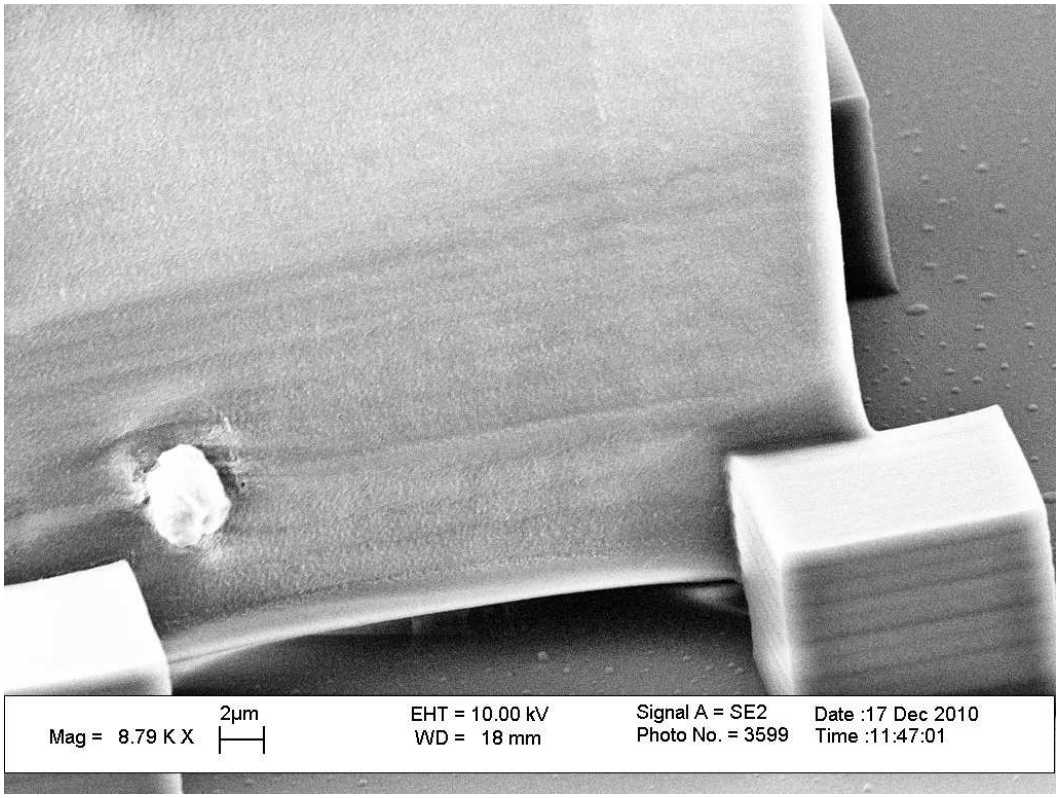

Figure 5.20:: SEM image showing a 0.2 µm z-spacing 40 µm cubic microresonator with 100 mM Coumarin 481. Additional parameters: P_{feet}=1.113 mW (440x512), P_{cube}=1.299 mW (440x512), 60x objective. The vertical surfaces of the cube are very smooth with the exception of the defect in the left corner. This defect occurred at the same place on other cubes within the same sample. (101213 IIIb-1)

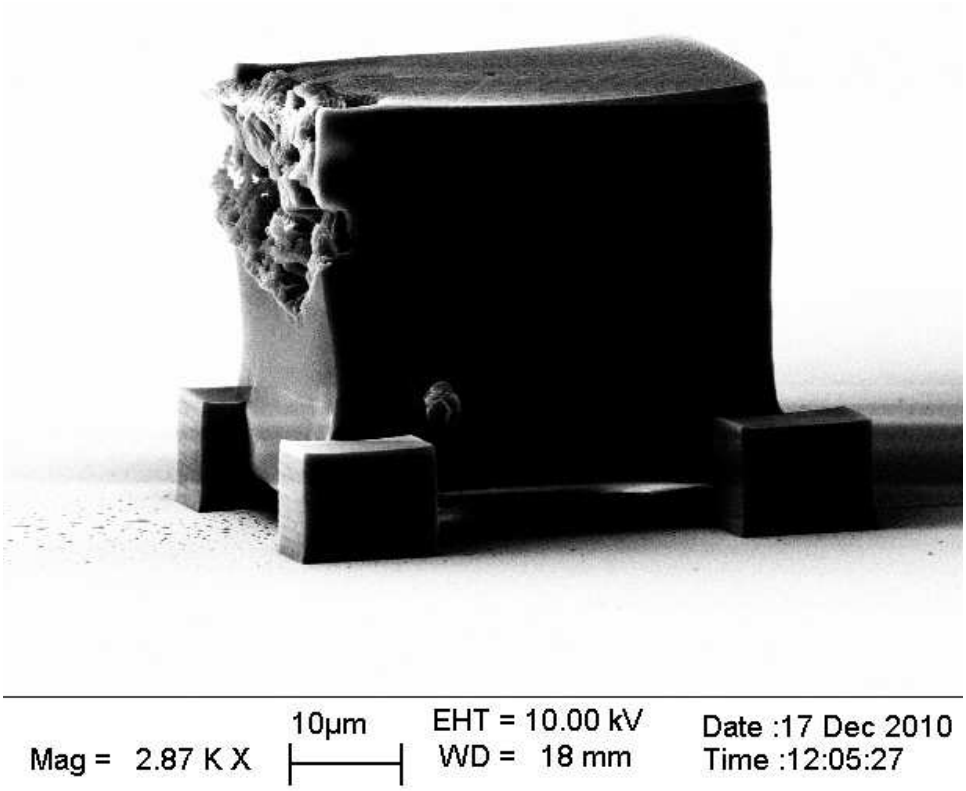

Figure 5.21: SEM image of a 40 µm cube showing large void. The location and size of the void was consistent across several microresonators. It is hypothesized that the consistently located voids are the result of inconsistent dose arising as an artifact of the raster scan system. Fabrication parameters are 0.2 µm z-step, 60x objective, 100 mM Coumarin 481 (101213 III-90a). P_{feet}=1.113 mW (440x512), P_{cube}=1.299 mW (440x512). Exceed boiling point of liquid. Use mask to cut off turn around part.

After unsuccessfully working for an extended period of time to eliminate the formation of large voids, the focus in microresonator fabrication shifted direction to create smaller microresonators with larger modal spacings. This shift was made over concerns about the ability to resolve fine features in a collected emission spectrum. As a result of changing fabrication dimensions from 40 to 10 µm, the predicted modal spacing near the Coumarin 481 emission maximum increased from 1.4 nm to 5.7 nm. The increased modal spacing would make it easier to observe the microcavity modes, if they exist, with a suitable spectrophotometer or monochromater for characterization.

10 µm cubic microresonators

Two representative 10 µm microresonator cubes elevated 10 µm off the glass substrate are shown in Figure 5.22. The overall cube shape is well formed and the support column is crisp (Figure 5.23). The most noticeable defect is the bulbous skirt around the bottom of the cube, see detail in figure 5.24. This is also the location where fabrication of the cube begins. A possible explanation for the skirt is that since the first few layers of the cube are unsupported during fabrication, they buckle and deflect until a sufficient number of layers have been attached to give the cube mechanical integrity. A likely workaround for this problem would be to fabricate the cubes in solid resin, where mobility of the thin polymerized layers would be minimal.

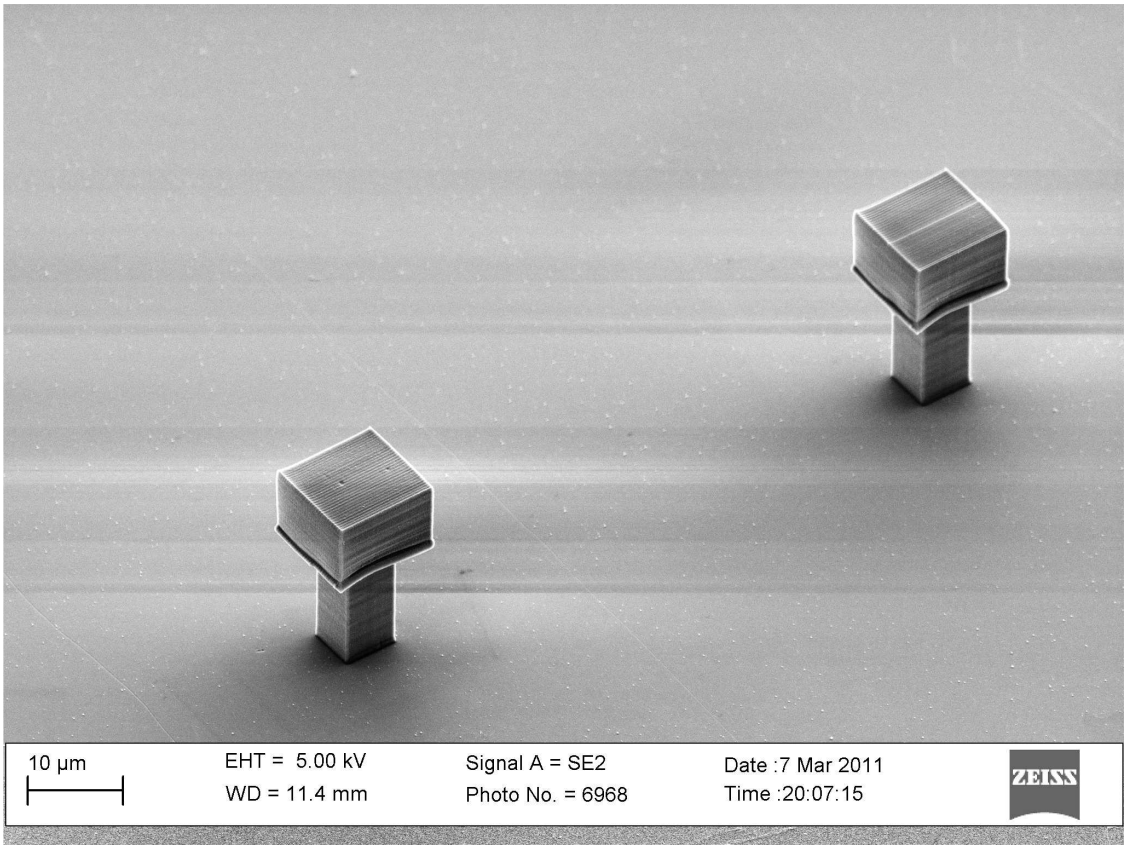

Figure 5.22: SEM image of two 10 μm cubic microresonators elevated 10 μm off a glass substrate. (depicted resonators are: 110227-3,4). Fabrication parameters: 100 mM Coumarin 481, 0.2 μm step, 60x objective. P_{top}=0.799 mW (z=45 (880x1024)), P_{column}=0.799 mW (z=30 880x1024)) from batch 110227.

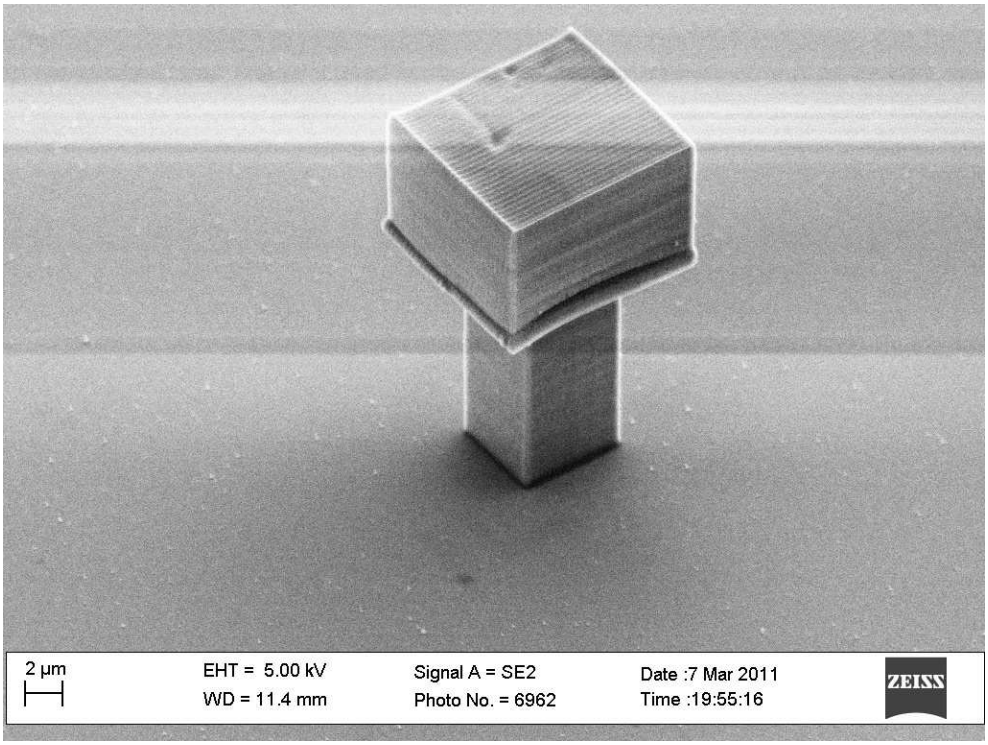

Figure 2.23: SEM image of a single 10 μm microresonator containing 100 mM Coumarin 481, 0.2 μm step, 60x objective. P_{top}=0.799 mW (z=45 (880x1024)), P_{column}=0.799 mW (z=30 880x1024)) from batch 110227. Note that indentations on top surface are SEM damage.

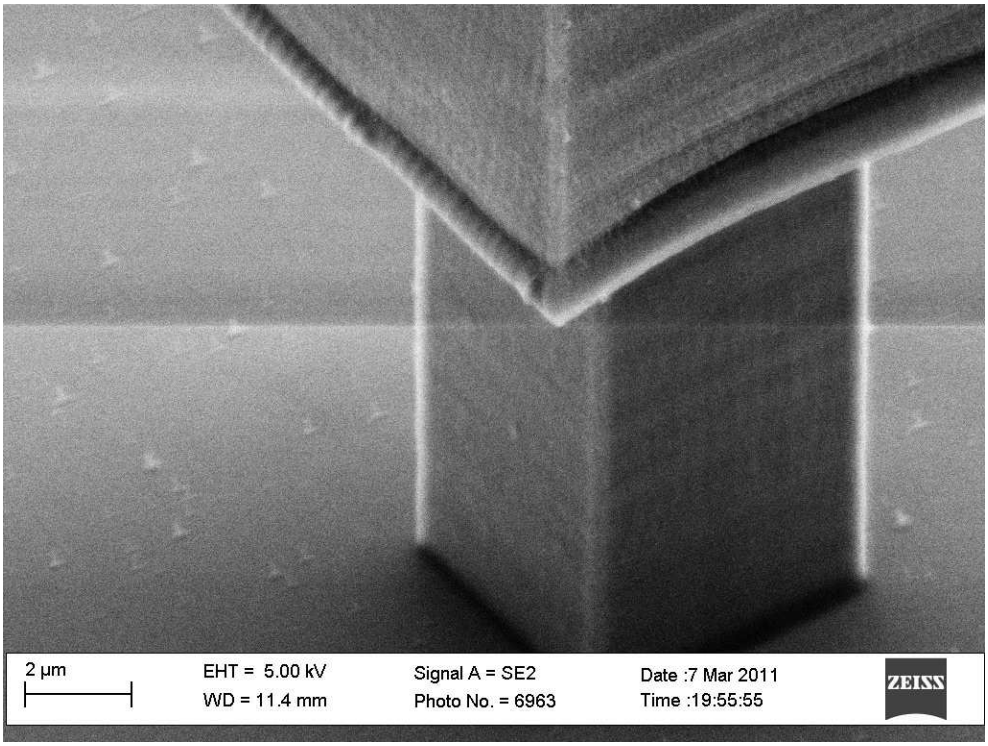

Figure 5.24: SEM detail of support column and bulbous skirt on bottom edge of 10 µm microresonator containing 100 mM Coumarin 481, 0.2 µm step, 60x objective. P_{top}=0.799 mW (z=45 (880x1024)), P_{column}=0.799 mW (z=30 880x1024)) from batch 110227.

CHAPTER 6: SPECTROSCOPIC CHARACTERIZATION

The single most important test of a microresonator is to observe its resonant modes via a modulated emission spectrum. This is achieved by first exciting the gain medium in the microresonator with an external high intensity light source (i.e. a laser) to cause emission. The population inversion causes stimulated emission, which in turn emits a sharp spectrum which can be measured in the far field. Two approaches were taken to measure the emission spectra of cubic microresonators.

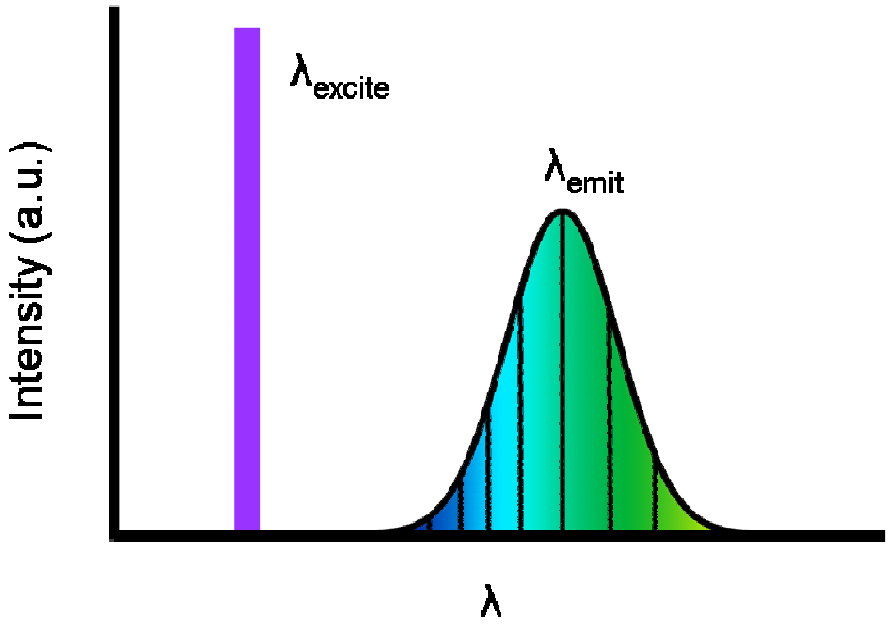

Figure 6.1: Schematic representation of a microresonator with an active gain medium with an emission spectrum represented by the Gaussian curve. A high energy excitation source, represented as a laser of wavelength λexcite causes stimulated emission of light with λemit as the wavelength of maximum intensity. Notice the overlapping vertical lines representing cavity modes inside of the emission spectrum.

The laboratory of Joseph Zyss at ENS Cachan has previously successfully measured emission spectra from a variety of 2D microresonators including squares, hexagons, circles and stadiums. Their setup utilizes a nanosecond 355 nm laser with 30 ps pulses at a 10 Hz repetition rate as the excitation source. The mean laser power was 9.5 mW with a peak power of 32 MW [35]. The laser beam is expanded to be many times larger than the microresonator under observation. The power distribution inside the excitation beam is Gaussian in nature; thus expanding the beam flattens the power distribution across the microresonator, which prevents the preferential excitation of resonant modes [4]. The microresonators are aligned to the excitation laser using a field microscope [36].

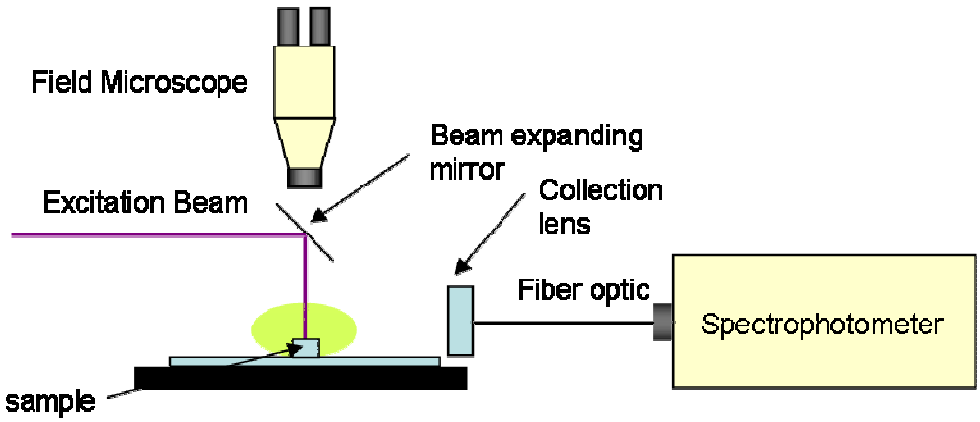

Figure 6.2: The spectroscopic characterization system at the Zyss Lab. The excitation source is a 405 nm picosecond laser with a 30 ps pulse width. Emitted light is collected from the structures via a collection lens fiber-coupled to a spectrophotometer.

To serve as a control and validate that the characterization setup was correctly functioning, the emission spectrum of an excited 40x40x10 μm Coumarin 481 doped cube was collected. The spectrum shows a continuous, non-modulated emission of fluorescence over a wide range of wavelengths, 450-540 nm. The Zyss group has not

indicated in published literature or private correspondence if collected emission spectra are corrected for the system response function.

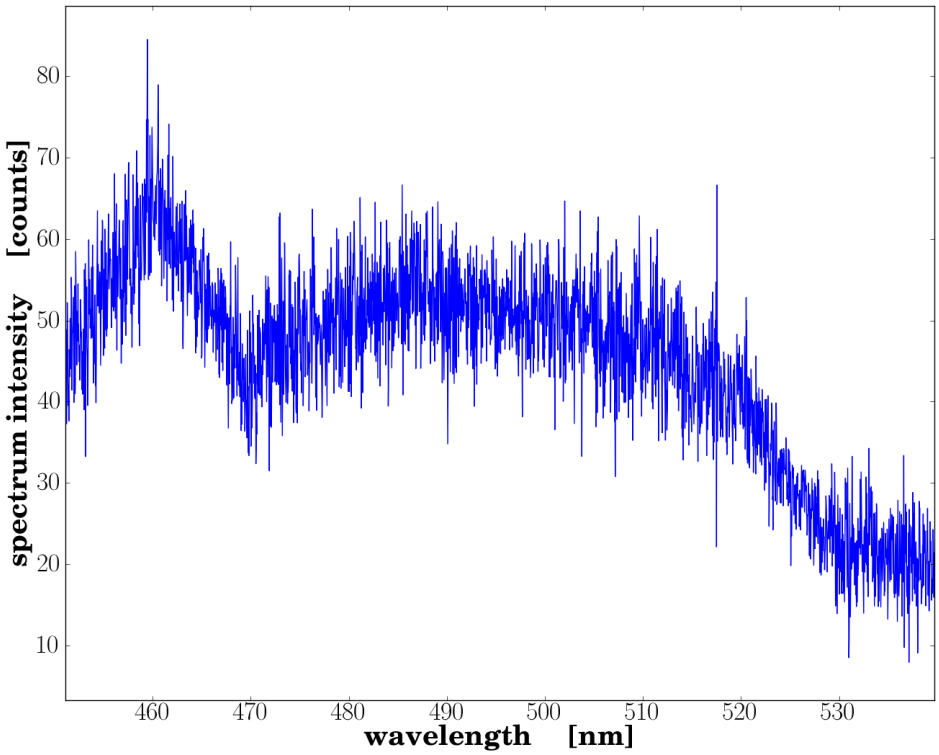

Figure 6.3: Fluorescence collected by Zyss research group at ENS Cachan from a 40x40x10 μm block doped with 100 mM Coumarin 481.

In comparison, seven spectra from a single 10 μm microresonator were collected; these spectra did demonstrate evidence of a sharply modulated emission spectrum. The best collected spectrum is show in figure 6.4. Due to the large peak power of the excitation laser, 32 MW, the magnitude of the collected spectra decreased rapidly as the Coumarin 481 suffered photobleaching.

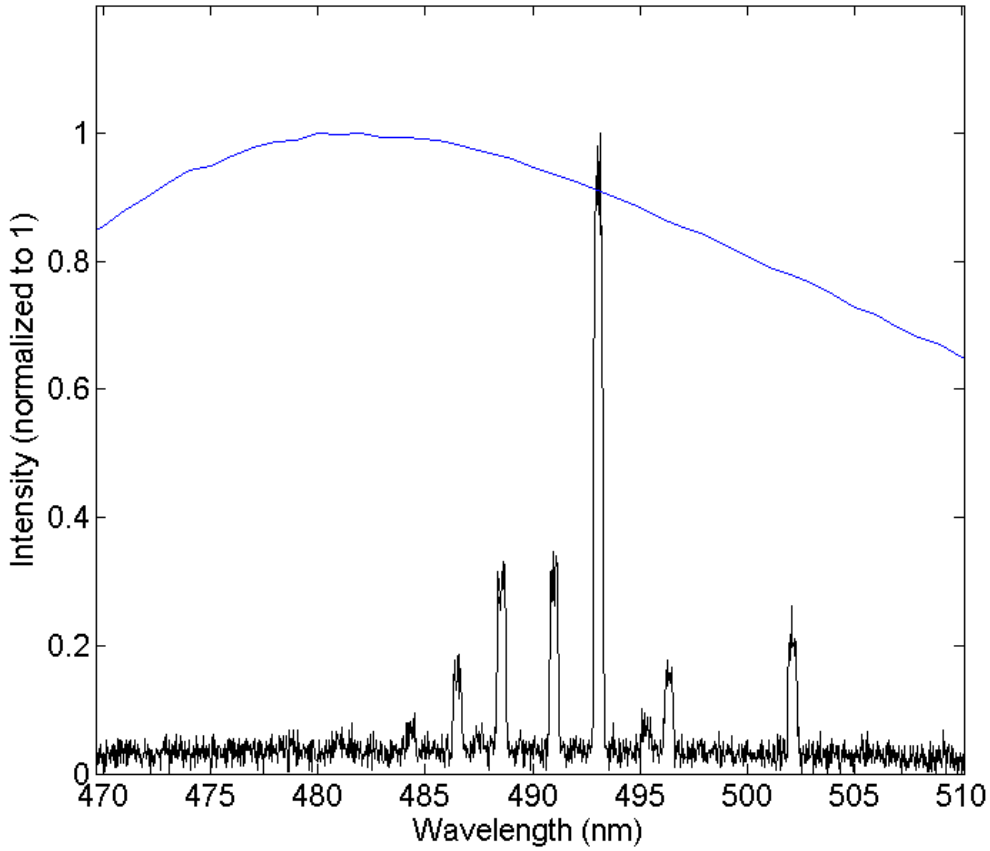

Figure 6.4: Emission spectrum collected from a single 10 μm microresonator doped with 100 mM Coumarin 481. The spectrum is overlaid with the emission spectrum of 100 mM Coumarin 481 as measured in a thin film. Microresonator excited by 355 nm nanosecond laser with 30 ps pulse width.

Table 6.1: Peak values, widths at half maximum, associated Q values and modal spacing.

Peak (nm)	Width at half max (nm)	Q	Modal Spacing (nm)
484.3	0.45	1100	2.21
486.509	0.39	1200	2.15
488.656	0.45	1100	2.30
490.951	0.45	1100	2.20
493.151	0.42	1200	2.05
495.2	0.51	1000	1.05
496.253	0.45	1100	5.75
502	0.42	1200	--
Mean	0.44	1100	2.53

The collected spectrum has eight modal peaks with a mean peak width of 0.44 nm with a standard deviation of 0.02 nm. The most intense mode is 493 nm. The mean width peak is very consistent with the relatively large spectrophotometer slit width. The mean apparent Q of the modes is 1100. The slit width limited resolution, in turn, places a lower boundary on the Q value, so that the mean Q of the modes is at least 1145, but possibly greater. In order to obtain higher resolution it will be necessary to amplify the emission signal collected. The modal spacing between the first six peaks is approximately 2.2 nm, but the spacing between the last three peaks is 1.05 and 5.75 nm.

In the theory chapter of this thesis, it was hypothesized that a cubic microresonator could be modeled as a square of comparable dimension. Based on this hypothesis, the predicted FSR for a 10 um cube is 5.7 nm. In the observed spectrum from the cube, only the distance between the final two observed peaks is equal to this value. The distance between the six four peaks is nearly half this value, which suggests that existence of modes with a path length twice that traveled in the square. One possible path could be a 4-node 3D orbit resembling the outline of the reception building of a 1960's Howard Johnson motel. However, the observed FSR could also be the additive effect of several different distinct orbits along their own planes. More research both in the lab and computationally will have to be done to better predict modal spacing in a cube.

In order to overcome the limitations of the Zyss setup, a second spectroscopic characterization setup was developed within the Perry research group. The Perry lab characterization setup is built of a similar overall design as that of the Zyss group, but is designed with high resolution (<0.1 nm) and noise rejection in mind. The excitation laser in the Perry setup is a continuous wave (CW) 405 nm diode laser with a peak powe of 30

mW. The laser beam is modulated by an optical chopper resulting in pulsed laser-like behavior. The rotational frequency of the optical chopper is fed as reference signal to a lock-in amplifier (Model 7265, Signal Recovery). The combination of these devices allows for significant improvement in the signal-to-noise ratio (SNR).

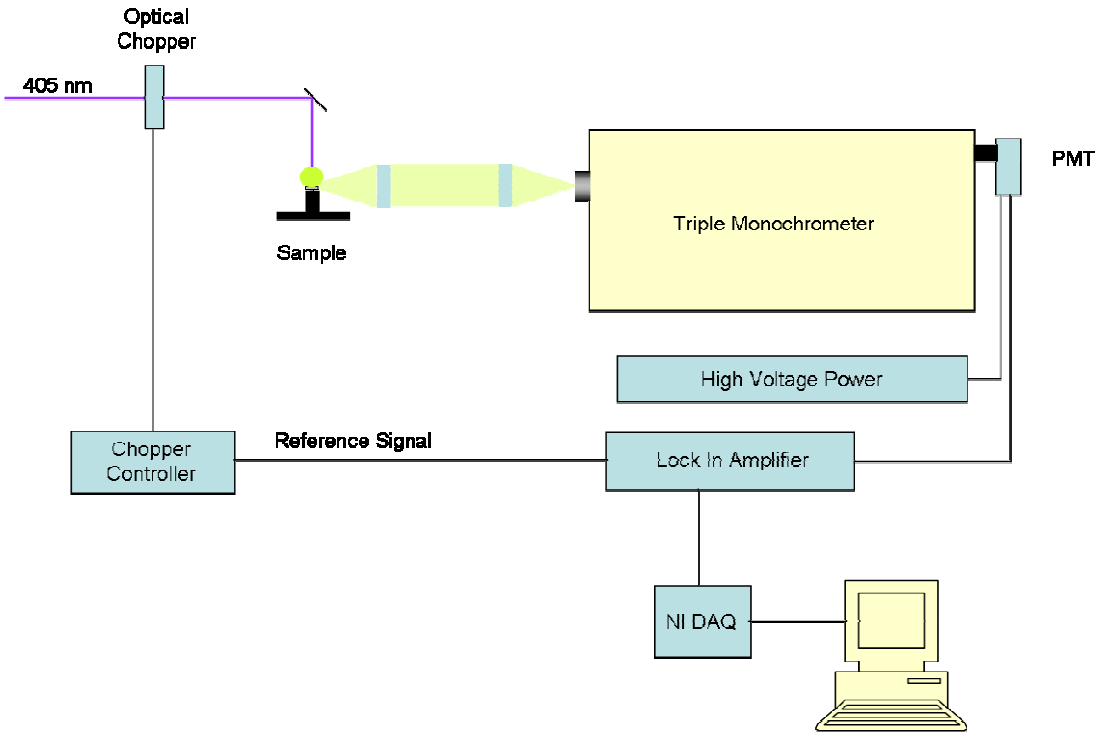

Figure 6.5: Perry group spectroscopic characterization setup, built to emphasize high resolution and high sensitivity.

Emitted fluorescence was directed to a triple monochrometer (Triplemate, SPEX) via a plano convex and convex lens collection setup. The first stage of the triple monochrometer is two Czerny-Turner monochrometers coupled to reject stray light. Given the 600 gr/mm gratings installed in this stage, it is possible to examine a bandwidth of up to 30 nm. Following the prefilter, the focused fluorescence travels into the final Czerny-Turner spectrograph and the fluorescence is focused on a 25 mm wide 1200 gr/mm grating with a spectral resolution of up to 0.035 nm [37].

The filtered light is collected by a photomultiplier tube (PMT) (Hamamatsu R928, Japan). A negative voltage of 500-800 V was applied to the cathode of the PMT from a high voltage power supply (Model PS325, Stanford Research Systems, Inc). The analog signal from the PMT was alternately monitored via an oscilloscope (TDS 220, Tekronix) or its signal feed into the lock in amplifier for synchronization with the optical chopper frequency.

Using the setup it was possible to get a strong signal from the emitted fluorescence from a single 10 μm cubic microresonator. However, the detected fluorescence, as seen on the oscilloscope, did not have sharp changes in intensity, but rather was uniform over the entire bandwidth of the triple monochrometer. This observation led to the conclusion that while the mean power of the CW 405 nm diode laser and the picosecond 355 nm laser were the same, 9.5 mW, the high peak energy of the pulsed laser was required to cause population inversion leading to stimulated emission in the microresonator. Determining the exact transition from spontaneous to stimulated emission in the microresonator via an optical emission intensity as a function of excitation power curve will be an important next step.

The presence of an energetic threshold for population inversion is only one of the defining three characteristics of a laser. The other two are the demonstration of spectral line narrowing, which was observed in the emission spectra collected by the Zyss group, and the emitted light from the device must be coherent. This last criterion was not measured in this work, but could be measured in future work by examining the directionality of emission as a function of angle relative to the microresonator. Given the

evidence, it seems reasonable to state that the microresonator is demonstrating stimulated emission.

CHAPTER 7: CONCLUSIONS AND FUTURE WORK

Conclusions

Cubic (10 μm on a side) microresonators of Coumarin 481 doped PMMA were created using MPL. An emissive dye, Coumarin 481, was integrated into the microresonators at 100 mM concentrations sufficient for achieving lasing. The periodic surface modulation of the microresonator side surfaces was reduced by decreasing the z-spacing between written planes of polymerized resin. The roughness of the top surface, arising from the raster scan process, was reduced via optimization of the raster line density.

The collected emission spectra from the 10 μm microresonators verified the existence of sharp resonant peaks. These sharp resonant peaks were only observed when the microresonators were excited with a high peak power, 32 MW, and not at an equivalent mean power, 9.5 mW, via a CW laser. The presence of this power dependence for the observation of resonant modes strongly suggests that the device has an energetic threshold for lasing and thus could be considered a microlaser if the emitted light from the device is demonstrated to be coherent.

It was previously predicted that the 3D cube could be generalized as a set of 2D square microresonators arranged at orthogonal directions. However, the measured modal spacing ($\delta\lambda \sim 2.5$ nm) between the peaks is half of what would be expected in a comparable 2D square microresonator (($\delta\lambda \sim 5.7$ nm). Additional experiments are necessary to collect spectra from a range of cube sizes to provide data to create a model to describe the modes in a cube.

Outlook

There are many promising areas for future study building off of this thesis.

Fabrication

The immediate next steps in fully understanding the relationship between modal spacing and cube dimension is to fabricate a series of cubes of varying edge lengths from 5, 10, 20 and 40 μm. The expected result is strong inverse correlation between microresonator size and modal spacing similar to the predicted behavior of a 2D square microresonator. The proposed sizes, 40 to 5 um, are within the fabrication capabilities of the Sutter-BioRad system utilized in this work.

Eventually it may become desirable to decrease microresonator size as small as 2 μm edge length. There are many advantages to creating smaller microresonators. First, as previously stated, there is an inverse relationship between microresonator volume and modal spacing. It follows that as the microresonator becomes sufficiently small it is possible to create a single mode microlaser. Second, reducing microresonator volume is a convenient approach for increasing the density of energy in the microresonator; this in turn increases the quality factor, Q.

In order to make the transition to 2 μm cubic microresonators, an alternate fabrication system with a higher degree of customizability should be employed. The XPS fabrication system in our lab is intended for high speed writing with 40 nm precision control over the exact position of the laser focal volume in the resin. With this system it will be possible to create microresonators with dimensions limited only by the laser voxel size. Additionally, since the laser shutter can operate at 10 Mhz, it will be possible to rapidly create arrays of microresonators to study optical coupling and other phenomena.

The fabricated microresonators, particularly the 10 μm, had smooth irregular features at the locations where writing of the cubes began. This is likely due to the

structural instability of single or small numbers of polymerized planes during the fabrication process. It is desirable to eliminate the formation of these soft features to reduce loss. An expedient method for reducing resin mobility during polymerization is reduce the potential mobility of the resin during polymerization by using a rigid blade cast film of acrylate monomers in lieu of a liquid resin. The blade cast films are similar in composition to the liquid resin used in these experiments except that the cast films contain a polymer binder, Poly(styrene-co-acrylonitrile), and dioxane as a solvent. The blade cast films also support the addition of an emissive dye.

Revisiting Coumarin 481

Experimental work has shown that Coumarin 481 doped microresonators photobleach within the course of a single data collection period. The rate of photobleaching can be slowed by reducing the peak power delivered to the microresonator to be only slightly over the energetic lasing threshold; the peak laser power could not be controlled with a high degree of finesse with the Zyss characterization setup, but control can be achieved. Further consideration should be put into finding an alternate more photostable dye.

Understanding Modal Structure

It is apparent that generalizing the 3D cube microresonator as a series of square planes with inscribed square modes fails to fully describe the modal structure of the cube. One possible approach to modeling the modal structure of the cube would be to develop a simple code iterating a billiard ball bouncing around inside a cube. The code of course

would have to consider the critical angle necessary for total internal reflection as well as total loss regions where all incident rays would extinguish. Such a code could be written as follows. First, it can be recognized that due to the symmetry of the cube, it is only necessary to have initial conditions on one face of the cube; thus it becomes possible to iterate initial conditions on one cube face rather than six. Second, as was observed while investigating the inscribed square mode of the square, the paths traced by angles close to the angle of the resonant mode converged to the stable path as the angle was slowly iterated. The observation of convergence from both negative and positive directions suggests that a machine learning algorithm could with training locate the resonant paths in a cubic microresonator. This process will likely be computationally intensive, but could be accomplished more rapidly with parallel processing.

There have been some symmetry based descriptions of modal structure of square microresonators as well as Finite Difference Time Domain (FDTD) simulations [12, 38]. There is also one published report modeling the electric field inside a 2um cubic microresonator; however, this publication treated the cube as a series of planes rather than a continuous entity [39]. The only practical consideration hindering modeling a cubic microresonator with FDTD is computational resources, which could be secured if funding were available.

Near Field v. Far Field

The resonant modes observed in the far field characterization systems in both the Zyss and Perry labs are lossy modes. The low loss modes are fully contained inside the microresonator and only apparent from outside via weak evanescent waves. The

evanescent waves are only observable in the near field, within λ/2 of the dye emission spectrum. The primary tool for examining the near field is Near Field Scanning Optical Microscopy (NSOM). NSOM is a thin (~100 nm) metal coated fiber optic probe that is scanned over the surface of a device at a distance of within λ/2. The light collected by the probe is processed to create an image of the evanescent field surrounding the device. This technique has two important limitations. First, positioning the probe accurately is no trivial matter on a 3D structure. Second, the placement of the probe in the near field of the device locally disturbs the electric field inside the device. The latter can be overcome in a 1-D waveguide by examining the input and output signals in and without the presence of the probe. However, implementing this method, known as Transmission NSOM (TNSOM) will be nontrivial for a 3D structure [40].

APPENDIX A: MATLAB CODES

Rowofblocks.m

```
%rowofblocks.m
%creates a row of blocks with configurable z-spacing, and regular x
positioning
%Created 2-2-11

clc
xspacing=80;
x0=0;
zspacing=[0.2]; %setting the length(zspacing)=1, creates only one block
y=0;
zinitial=0;
zheight=20;
zneg=-10; %sign of this number is flipped in subsquent line; hence to
create a block from 10 to -5, zneg=-10
t=5000;
tpause=2000;
fid=fopen('bob.txt','w');
for k=0:length(zspacing)-1
    x=k*xspacing+x0;
    zspan=zneg:zspacing(k+1):zheight;
    for j=1:length(zspan)
        z=-zspan(j);
       fprintf(fid,'%6.2f \t %6.2f \t %6.2f \t %6.1f \t 1 \n',x,
y,z,t);
       fprintf(fid,'%6.2f \t %6.2f \t %6.2f \t %6.1f \t 0 \n',x,
y,z,tpause);
    end
end
```

Resonant2.m

```
%Resonant2.m
%Examines the problem of resonance only at integer multiples of the
%pathlength in a 2D Square. This script improves on the existing
Resonantmode1.m
%Created by Eric Mansfield
%Created on 12/7/10
clear
clc
siderange=[5 10 20 40 60 80 100];
n=1.45;
m=1:1:2000;
lambdadata=[];
modalspacing=[];
for j=1:length(siderange)
    side=siderange(j);
    diagonal=(side/2)*sqrt(2);
```

```
    pathlength=(4*diagonal);
    resonantmodes=[];

   for k=1:length(m)
       lambda=n.*pathlength./k;
       lambdadata(j,k)=lambda;
       if k>=2
           modalspacing(j,k-1)=abs(lambdadata(j,k)-lambdadata(j,k-1));
       else
       end
   end
end
plot(lambdadata,m,'s')
axis([0.1 1 0 m(end)])
ylabel('Integer multiple m')
xlabel('Wavelength (um)')
figure(2)
lambdadata=lambdadata.*1000;
modalspacing=modalspacing.*1000;
% lambdadata(2:end,:)=lambdadata(2:end,:)*1000;
plot(lambdadata(1,2:end),modalspacing(1,:),'s',lambdadata(2,2:end),moda
lspacing(2,:),'s'...

,lambdadata(3,2:end),modalspacing(3,:),'s',lambdadata(4,2:end),modalspa
cing(4,:),'s',...

lambdadata(5,2:end),modalspacing(5,:),'s',lambdadata(6,2:end),modalspac
ing(6,:),'s',lambdadata(7,2:end),modalspacing(7,:),'s')
legend('5um side','10um side','20um side','40um side','60um side','80um
side','100um side',2)
axis([200 1000 0 10])
ylabel('Modal Spacing (nm)')
xlabel('Wavelength (nm)')
title('Modal Spacing as a function of edge length')
```

SquarePlanarRayTrace.m

```
%SquarePlanarRayTrace.m
%Eric Mansfield
%Created 5-24-10
%Changes coordinates to all be relative, so ray is a function of x,y,
and
%theta.
%Traces rays inside a square
%BEST COPY
clear
clc
%Inputs
n1=1;
n2=1.492; %For continuous PMMA
Thetao=89; %Theta Incident on outer surface
```

```
L1=10; %Length of polygon side 1
L2=10; %length of polygon side 2
f=.5; %Fraction of L1 measured from bottom, representing entry point of
ray.
Thetacrit=real(asin(n1/n2));
InDeg=Thetacrit*180/pi;
rayhealth=1; %Binary value coding for ray existence
i=1; %inital counter

%Finding Theta(i) with Snell's Law (Theta is henceforth in Radians)
Theta(i)=46*pi/180;%asin(n1*sind(Thetao)/n2);
rayX(i)=0;
rayY(i)=f*L1;
perpx=[];
bounceplane=[];

while (rayhealth==1) & (i<=20)
    i=i+1;
    Theta(i)=-Theta(i-1);
    planeI=tan(Theta(i-1))*(-rayX(i-1))+rayY(i-1); %rayY(i)
    planeII=-rayY(i-1)/tan(Theta(i-1))+rayX(i-1); %rayX(i)
    planeIII=tan(Theta(i-1))*(L2-rayX(i-1))+rayY(i-1); %rayY(i)
    planeIV=(L1-rayY(i-1))/tan(Theta(i-1))+rayX(i-1); %rayX(i)

    if ((planeI~=rayY(i-1)) & (planeI<=L1) & (planeI>=eps))
        rayY(i)=planeI;
        rayX(i)=0;
        bounceplane=1;
    elseif ((planeII~=rayX(i-1)) & (planeII<=L2) & (planeII>=eps))
        rayX(i)=planeII;
        rayY(i)=0;
        bounceplane=2;
    elseif ((planeIII~=rayY(i-1)) & (planeIII<=L1) & (planeIII>=eps))
        rayY(i)=planeIII;
        rayX(i)=L2;
        bounceplane=3;
    elseif ((planeIV~=rayX(i-1)) & (planeIV<=L2) & (planeIV>=eps))
        rayX(i)=planeIV;
        rayY(i)=L1;
        bounceplane=4;
    else %Corners
        display('Corner')
        rayhealth=0;
        bounceplane=5;
    end

    %Does complete loss occur?
    if ((bounceplane==1) || (bounceplane==3))
        if (abs(Theta(i))) <= Thetacrit
            display('Total Loss')
            rayhealth=0;
        elseif (abs(Theta(i))) > Thetacrit
            rayhealth=1;
        else
        end
    elseif ((bounceplane==2) || (bounceplane==4))
```

```
        if (pi/2-abs(Theta(i))) <= Thetacrit
            display('Total Loss')
            rayhealth=0;
        elseif (pi/2-abs(Theta(i))) > Thetacrit
            rayhealth=1;
        else
        end
    else
        display('Complete Loss in corner')
        rayhealth=0;
    end
end

plot(rayX,rayY)
axis([0 L1 0 L2])
axis square
xlabel('Dimensionless Length')
ylabel('Dimensionless Height')
```

ModalSpacing.m

```
%ModalSpacing in a 1-D Resonator
%Examines the problem of resonance only at integer multiples of the
%pathlength. This script improves on the existing Resonantmode1.m
%Created by Eric Mansfield
%Created on 4/20/11
clear
clc
siderange=[15 25 30 50 70 90 110]%[5 10 20 40 60 80 100];
n=1.45;
m=1:1:2000;
lambdadata=[];
modalspacing=[];
for j=1:length(siderange)
    side=siderange(j);
    pathlength=(2*side); %side is length
    resonantmodes=[];

   for k=1:length(m)
        lambda=n.*pathlength./k;
        lambdadata(j,k)=lambda;
        if k>=2
            modalspacing(j,k-1)=abs(lambdadata(j,k)-lambdadata(j,k-1));
        else
        end
   end
end
% plot(lambdadata,m,'s')
% axis([0.1 1 0 m(end)])
% ylabel('Integer multiple m')
% xlabel('Wavelength (um)')
% figure(2)
lambdadata=lambdadata.*1000;
modalspacing=modalspacing.*1000;
% lambdadata(2:end,:)=lambdadata(2:end,:)*1000;
```

```
plot(lambdadata(1,2:end),modalspacing(1,:),'s',lambdadata(2,2:end),moda
lspacing(2,:),'s'...

,lambdadata(3,2:end),modalspacing(3,:),'s',lambdadata(4,2:end),modalspa
cing(4,:),'s',...

lambdadata(5,2:end),modalspacing(5,:),'s',lambdadata(6,2:end),modalspac
ing(6,:),'s',lambdadata(7,2:end),modalspacing(7,:),'s')
legend('5um length','10um length','20um length','40um length','60um
length','80um length','100um length',2)
axis([200 1000 0 20])
ylabel('Modal Spacing (nm)')
xlabel('Wavelength (nm)')
title('Modal Spacing as a function of 1-D cavity length')
```

REFERENCES

1. Saleh, B.E.A. and M.C. Teich, *Fundamentals of photonics*. 2nd ed. Wiley series in pure and applied optics. 2007, Hoboken, N.J.: Wiley-Interscience. xix, 1177 p.
2. Vahala, K.J., *Optical microcavities.* Nature, 2003. **424**(6950): p. 839-846.
3. O'Shea, D.C., W.R. Callen, and W.T. Rhodes, *Introduction to lasers and their applications*. 1977, Reading, Mass.: Addison-Wesley Pub. Co. xii, 276 p.
4. Lebental, M., et al., *Inferring periodic orbits from spectra of simply shaped microlasers.* Physical Review A, 2007. **76**(2): p. 023830.
5. Armani, D.K., et al., *Ultra-high-Q toroid microcavity on a chip.* Nature, 2003. **421**(6926): p. 925-928.
6. Gorodetsky, M.L., A.A. Savchenkov, and V.S. Ilchenko, *Ultimate Q of optical microsphere resonators.* Opt. Lett., 1996. **21**(7): p. 453-455.
7. Vollmer, F., S. Arnold, and D. Keng, *Single virus detection from the reactive shift of a whispering-gallery mode.* Proceedings of the National Academy of Sciences, 2008. **105**(52): p. 20701-20704.
8. Bhushan, B., *Springer handbook of nanotechnology*. 2010, Springer: Berlin ; New York. p. 1 online resource (xlviii, 1961 p.).
9. Haske, W., et al., *65 nm feature sizes using visible wavelength 3-D multiphoton lithography.* Opt. Express, 2007. **15**(6): p. 3426-3436.
10. Cumpston, B.H., et al., *Two-photon polymerization initiators for three-dimensional optical data storage and microfabrication.* Nature, 1999. **398**(6722): p. 51-54.
11. Poon, A.W., F. Courvoisier, and R.K. Chang, *Multimode resonances in square-shaped optical microcavities.* Opt. Lett., 2001. **26**(9): p. 632-634.
12. Wei-Hua, G., et al., *Modes in square resonators.* Quantum Electronics, IEEE Journal of, 2003. **39**(12): p. 1563-1566.
13. Mahon, R., T.J. McLlrath, and D.W. Koopman, *High-power TEM00 tunable laser system.* Appl. Opt., 1979. **18**(6): p. 891-896.
14. Maeda, M. and Y. Miyazoe, *Flashlamp-Excited Organic Liquid Laser in the Range from 342 to 889 nm*. Japanese Journal of Applied Physics, 1972. **11**(5).
15. Pierce, B. and R. Birge, *Lasing properties of several near-IR dyes for a nitrogen laser-pumped dye laser with an optical amplifier.* Quantum Electronics, IEEE Journal of, 1982. **18**(7): p. 1164-1170.
16. Webb, J., F. Webster, and B. Plourde, *Sixteen new infrared laser dyes excited by a simple, linear flashlamp.* Quantum Electronics, IEEE Journal of, 1974. **10**(9): p. 696-697.
17. Hammond, P.R., *Laser dye DCM, its spectral properties, synthesis and comparison with other dyes in the red.* Optics Communications, 1979. **29**(3): p. 331-333.
18. Exciton Corporation. *DCM*. 2010 [cited 2011; Available from: http://exciton.com/pdfs/DCM%202010.pdf.
19. Schimitschek, E., et al., *New improved laser dye for the blue-green spectral region.* Quantum Electronics, IEEE Journal of, 1973. **9**(7): p. 781-782.

20. Exciton Corporation. *Coumarin 481*. 2010 [cited 2011; Available from: http://exciton.com/pdfs/c481.pdf.
21. Eschrich, T.C. and T.J. Morgan, *Dye laser radiation in the 370?760-nm region pumped by a XeF excimer laser.* Appl. Opt., 1985. **24**(7): p. 937-938.
22. Exciton Corporation. *Bis-MSB*. 2010 [cited 2011; Available from: http://exciton.com/pdfs/bismsb.pdf.
23. Reynolds, G.A. and K.H. Drexhage, *New coumarin dyes with rigidized structure for flashlamp-pumped dye lasers.* Optics Communications, 1975. **13**(3): p. 222-225.
24. Bos, F., *Optimization of spectral coverage in an eight-cell oscillator-amplifier dye laser pumped at 308 nm.* Appl. Opt., 1981. **20**(20): p. 3553-3556.
25. Exciton Corporation. *Coumarin 540A*. 2010 [cited 2011; Available from: http://exciton.com/pdfs/c540a.pdf.
26. Uchino, O., et al., *Efficient dye lasers pumped by a XeCl excimer laser.* Applied Physics A: Materials Science & Processing, 1979. **19**(1): p. 35-37.
27. P. A. Fleitz, C.J.S., R. N. Steppel, J. M. Kauffman, C. J. Kelly, A. Ghiorghis, *Characterization of New Excimer Pumped UV Laser Dyes 2. p-Quaterphenyls.* Laser Chemistry, 1991. **11**(2).
28. Exciton Corporation. *p-Terphenyl*. 2010 [cited 2011; Available from: http://exciton.com/pdfs/ptp.pdf.
29. Exciton Corporation. *Rhodamine 590*. 2010 [cited 2011; Available from: http://exciton.com/pdfs/RH590.pdf.
30. Exciton Corporation. *LD 466*. 2010 [cited 2011; Available from: http://exciton.com/pdfs/ld466.pdf.
31. Schimitschek, E.J., et al., *Laser performance and stability of fluorinated coumarin dyes.* Optics Communications, 1974. **11**(4): p. 352-355.
32. Binnig, G., C.F. Quate, and C. Gerber, *Atomic Force Microscope.* Physical Review Letters, 1986. **56**(9): p. 930.
33. Deegan, R.D., et al., *Capillary flow as the cause of ring stains from dried liquid drops.* Nature, 1997. **389**(6653): p. 827-829.
34. Lensen, M.C., et al., *Aided Self-Assembly of Porphyrin Nanoaggregates into Ring-Shaped Architectures.* Chemistry – A European Journal, 2004. **10**(4): p. 831-839.
35. LaFargue, C., *Samples Sent to France*, E. Mansfield, Editor. 2011. p. 16.
36. Lebental, M., *Chaos quantique et micro-lasers oraniques*. 2007, L'Universitie Paris XI: Cachan. p. 197.
37. SPEX Industries, *Triplemate: Unique, Optically Fast, Rugged, Triple Spectrograph*. 1981. p. 4.
38. Wei-Hua, G., et al., *Whispering-gallery-like modes in square resonators.* Quantum Electronics, IEEE Journal of, 2003. **39**(9): p. 1106-1110.
39. Okada, K., et al., *Resonance Modes in Si Micro-Cubic Cavity Coupled with Ge:SiO Waveguide.* Japanese Journal of Applied Physics, 2006. **45**(8B): p. 6663-6666.
40. Ridder, R.M., W.C.L. Hopman, and E.J. Klein, *Characterization Techniques for Planar Optical Microresonators*, in *Photonic Crystals: Physics and Technology*, C. Sibilia, et al., Editors. 2008, Springer Milan. p. 193-216.